

JOINT ANALYSIS OF CLUSTER OBSERVATIONS: I. MASS PROFILE OF ABELL 478 FROM COMBINED X-RAY, SUNYAEV-ZEL'DOVICH, AND WEAK LENSING DATA

ANDISHEH MAHDAVI, HENK HOEKSTRA AND ARIF BABUL

Department of Physics and Astronomy, University of Victoria, Victoria, BC V8W 3P6, Canada

JONATHAN SIEVERS

Canadian Institute for Theoretical Astrophysics, 60 St. George St., Toronto, ON M5S 3H8, Canada

STEVEN T. MYERS

National Radio Astronomy Observatory, 1003 Lopezville Rd., Socorro, NM 87801

AND

J. PATRICK HENRY

Institute for Astronomy, 2680 Woodlawn Drive, Honolulu HI 96822, U. S. A.

Submitted May 16, 2006; Accepted March 2, 2007 for publication in The Astrophysical Journal

ABSTRACT

We provide a new framework for the joint analysis of cluster observations (JACO) using simultaneous fits to X-ray, Sunyaev-Zel'dovich (SZ), and weak lensing data. Our method fits the mass models simultaneously to all data, provides explicit separation of the gaseous, dark, and stellar components, and—for the first time—allows joint constraints on all measurable physical parameters. JACO includes additional improvements to previous X-ray techniques, such as the treatment of the cluster termination shock and explicit inclusion of the BCG's stellar mass profile. An application of JACO to the rich galaxy cluster Abell 478 shows excellent agreement among the X-ray, lensing, and SZ data. We find that Abell 478 is consistent with a cuspy dark matter profile with inner slope $n = 1$. Accounting for the stellar mass profile of the BCG allows us to rule out inner dark matter slopes $n > 1.1$ at the 99% confidence level. At large radii, an r^{-3} asymptotic slope is preferred over an r^{-4} behavior. All single power law dark matter models are ruled out at greater than the 99% confidence level. JACO shows that self-consistent modeling of multiwavelength data can provide powerful constraints on the shape of the dark profile.

Subject headings: Dark matter—X-rays: galaxies: clusters—gravitational lensing—galaxies: clusters: individual (Abell 478)

1. INTRODUCTION

N-body simulations of our Cold Dark Matter (CDM) dominated universe suggest that evolved galaxies and clusters of galaxies are contained in dark halos with self-similar density profiles. In the collisionless limit, $\rho_{\text{dm}}(r/r_d)/\delta = f(x)$. The characteristic density δ and radius r_d depend on the halo mass and the cosmological parameters, but the normalized profile $f(x)$ itself does not (Navarro, Frenk, & White 1997; Moore et al. 1998; Ghigna et al. 2000; Subramanian, Cen, & Ostriker 2000; Fukushige & Makino 2001; Williams, Babul, & Dalcanton 2004; Merritt et al. 2005). The robustness with which collisionless N-body simulations predict a universal profile makes the observational measurement of $f(x)$ particularly important. If we are to be satisfied that our understanding of hierarchical structure formation is correct, we need to use the best available data to test the theoretical dark matter profiles in detail.

Observations of $f(x)$ also have implications for self-interacting dark matter (SIDM) as an alternative to the collisionless models. If the weak interaction cross section of the particles in a halo is large enough, substantial effects on the shape of the density profile should appear within a Hubble time. Initially cuspy profiles should evolve constant-density cores with a size $\sim 3\%$ of the virial radius (Spergel & Steinhardt 2000; Burkert 2000). It is an open question whether the SIDM cores are stable and long-lived enough to be observable (Bal-

berg, Shapiro, & Inagaki 2002; Ahn & Shapiro 2005) or whether the cores quickly collapse, forming an r^{-2} isothermal cusp (Kochanek & White 2000). If the cores are stable, measurements of $f(x)$ can provide constraints on the interaction cross section and hence on the nature of dark matter itself.

Rich, $\gtrsim 10^{14} M_\odot$ clusters of galaxies are excellent laboratories for the measurement of $f(x)$ because of the large number of independent techniques available for mass measurement. In this series of papers, we examine the complex task of constraining $f(x)$ *simultaneously* using the X-ray emitting intracluster medium (ICM), the Sunyaev-Zel'dovich decrement, and weak gravitational lensing maps. For the joint analysis of cluster observations (JACO), we always begin with separate luminous and dark mass profiles, and calculate the observables—the X-ray spectrum, the SZ decrement, or the tangential lensing shear—directly from the underlying physical model. In other words, our fits always take place in the data space, rather than in mass, density or temperature space. This approach allows for (1) deformation of the theoretical profiles to account for the appropriate instrumental degradation at each wavelength and (2) the ability to combine lensing, SZ, and X-ray data in a single grand total fit.

Other works have examined the multiwavelength approach. Miralda-Escude & Babul (1995) carried out the first comparison of physical X-ray and strong lensing models for a sample of three rich clusters; Squires

et al. (1996) extended the comparison to weak lensing. Zaroubi et al. (1998) and Zaroubi et al. (2001), using idealized X-ray and SZ observations of simulated clusters, showed that the unique axisymmetric deprojection of the gas density profile is possible by combining the two types of data. Doré et al. (2001), also using simulated clusters, argued that the simultaneous deprojection of SZ and weak lensing data is sensitive to the noise properties of the data. De Filippis et al. (2005) and Sereno et al. (2006) use combined X-ray and SZ data to place constraints on the triaxiality and inclination of the intracluster medium assuming that they are single-component, isothermal systems; they do not attempt to constrain the dark profile. Assuming a Navarro et al. (1997) mass profile, LaRoque et al. (2006) use joint X-ray and SZ data from 38 clusters to constrain the gas mass fraction.

JACO is the first method to use X-ray, SZ, and weak lensing data simultaneously to constrain the shape of the dark matter profile in clusters. This paper describes a test of this method on the cluster Abell 478. Chief among the assumptions allowing the extraction of the dark matter profile is that the gas in hydrostatic equilibrium with the overall gravitational potential. If hydrostatic equilibrium is strongly violated, then determination of the structure of the dark halo from the X-ray data alone becomes difficult. Because ongoing or recent cluster mergers are common, the identification of clusters that are as close to prototypical (or “boring”) as possible is valuable for detailed mass measurement. The difficulty of finding systems suitable for hydrostatic analysis is evident in the latest Chandra and XMM-Newton studies of relaxed clusters.

Clusters that appeared smooth and relaxed before Chandra and XMM-Newton observations often contain features that make them unfit for equilibrium analysis. Examples include cold fronts (Vikhlinin, Markevitch, & Murray 2001; Bialek, Evrard, & Mohr 2002; Dupke & White 2003; Hallman & Markevitch 2004) or shocks (Markevitch & Vikhlinin 2001; Markevitch et al. 2002; Fabian et al. 2003; Fujita et al. 2004) in recent mergers. In clusters with X-ray substructure, the use of hydrostatic equilibrium may yield incorrect results (Poole et al. 2006). In many otherwise seemingly relaxed clusters, heating by a central AGN is required to reconcile the short cooling times with the deficit of $kT \lesssim 1$ keV gas in the quantities predicted by quasihydrostatic cooling flow models (Tamura et al. 2001; Fabian et al. 2001; Matsushita et al. 2002; Peterson et al. 2003; Kaastra et al. 2004; Voit & Donahue 2005). Gas in the region directly affected by the AGN is unlikely to be in hydrostatic equilibrium, and the equilibrium equations may yield incorrect results.

The most recent work shows, however, that many clusters can be successfully modeled as equilibrium systems outside the region of influence of the central AGN. In these regions, the total density distribution frequently resembles a pure $n = 1$ Navarro et al. (1997) profile, and either a single or double β -model provides a successful description of the X-ray surface brightness (Schmidt, Allen, & Fabian 2001; Arabadjis, Bautz, & Garmire 2002; Allen, Schmidt, & Fabian 2002; Lewis, Buote, & Stocke 2003; Buote & Lewis 2004; Pointecouteau et al. 2004; Buote, Humphrey, & Stocke 2005; Gavazzi 2005;

Pointecouteau, Arnaud, & Pratt 2005; Vikhlinin et al. 2006). However, in a few cases, evidence for a significantly shallower $n \lesssim 0.5$ (Ettori et al. 2002; Sander-son, Finoguenov, & Mohr 2005; Voigt & Fabian 2006) exists, echoing similar results in several strong gravitational lensing studies (Tyson, Kochanski, & dell’Antonio 1998; Sand, Treu, & Ellis 2002; Sand et al. 2004).

The substantial progress allowed by Chandra and XMM-Newton data leads us to consider whether the constraints on the dark matter structure could benefit from a refinement of the mass fitting technique and the use of optical and radio data in a simultaneous fit. In this paper we show that through the use of a multiwavelength modeling technique specifically aimed at constraining the dark matter (as opposed to the total) mass profile, enhanced constraints on the slope of the dark mass distribution in clusters are possible. In §2 we motivate the technique and describe it in detail. We apply the technique to the rich cluster Abell 478 in §3, and compare the results with previous work and N-body models in §4. We conclude in §5.

2. METHOD

2.1. General Principles

The purpose of JACO is to constrain the shape of the dark matter profile in clusters of galaxies via a single multi-parameter fit to X-ray, lensing, and Sunyaev-Zel’dovich data. The broad features of our technique are:

Separation of the mass model into the gaseous, stellar, and dark components. Rather than fitting for the total gravitating mass, JACO splits the potential into three separately modeled components, thus guaranteeing their positivity. As a result JACO is incapable of generating unphysical mass profiles as is sometimes the case with parameterized X-ray temperature profiles (Pizzolato et al. 2003; Buote & Lewis 2004). The stellar mass contributes a substantial part of the gravitating mass within 3% of the cluster virial radius (Sand et al. 2004), an important but sometimes neglected effect when testing for the presence of a SIDM constant density core.

Direct constraints from uncorrelated data. We conduct minimal data processing. We use the mass models to calculate, project, and PSF-distort theoretical spectra, and then fit these to the measured X-ray count spectra. We avoid deprojecting the data, thus guaranteeing fits to uncorrelated data. The gas temperature is handled as an internal variable, so that we skip the temperature fitting stage altogether. For Sunyaev-Zel’dovich measurements, we calculate and fit the uncorrelated Fourier modes of the decrement directly.

No X-ray temperature weighting. Because the mass models are fit directly to the spectra there is no need to calculate emission- or otherwise-weighted temperatures. Hydrodynamic N-body simulations show that emission-weighted temperatures do not accurately reflect the measured spectroscopic temperature (Mazzotta et al. 2004; Rasia et al. 2005); recent methods for getting around this problem require the calculation of theoretical weights that depend on the X-ray calibration files (Vikhlinin 2006). JACO calculates 2D spectra directly from the mass models. Temperature and density variations within any given annulus are reflected in the projected 2D X-ray spectra without any emission weighting.

What is truly new here is (1) the direct calculation of

X-ray spectra from the gravitational potential, (2) the use of this potential to model Sunyaev-Zel'dovich and weak lensing observations simultaneously, and (3) the ability to conduct a full, covariant error analysis on all the physical parameters. There are also other important features that have not been implemented in any prior method, e.g. the strict calculation of the mean molecular weight from the metallicity profile (§2.2) and the formal modeling for the termination shock as the cluster boundary (§2.3). Some of the other aspects of JACO have been discussed before. For example, Markevitch & Vikhlinin (1997) separate the gravitational potential into gaseous and dark components when modeling Abell 2256. Fukazawa et al. (2006) and Humphrey et al. (2006) employ the stellar profile of the BCG in the X-ray fit. And “Smaug” (Pizzolato et al. 2003) was the first technique to incorporate direct fitting of projected spectra. JACO improves on Smaug by fitting a complete physical model, and avoiding the use of emission-weighted temperatures and coarsely gridded cooling functions. While JACO incorporates relevant ideas from its predecessors, it was written completely independently, as the physical motivation behind JACO made reuse of other code either slow or impossible.

2.2. Fundamental Equations

We first write the emissivity of the intracluster plasma,

$$\epsilon_\nu = n_e n_H \lambda_\nu(T, Z) = \left\langle \frac{n_e}{n_H} \right\rangle n_H^2 \lambda_\nu(T, Z), \quad (1)$$

where T is the temperature, n_e is the electron density, and n_H is the hydrogen nucleus density. The cooling function $\lambda_\nu(T, Z)$ is weighted over all metals with relative abundances fixed on the Grevesse & Sauval (1998) scale; in this system the absolute abundance is Z . For λ_ν , JACO users can choose between the APEC and the MEKAL plasma codes, or they can provide their own. Note that in ionization equilibrium $\langle n_e/n_H \rangle$ is a function of metallicity; JACO recalculates it each time it derives an X-ray spectrum for a new value of Z . The same applies to the mean molecular weight μ . We find that if we did not recalculate μ and $\langle n_e/n_H \rangle$ each time (i.e., held them fixed at some fiducial \bar{Z}), we would be making up to a 5% systematic error in the output spectrum.

In the approximation that the cluster contains a relaxed, spherical, and stationary ideal gas,

$$\frac{1}{\rho_g} \frac{d}{dr} \left(\frac{\rho_g kT}{\mu m_p} \right) = - \frac{G(M_d + M_g + M_s)}{r^2}. \quad (2)$$

where m_p is the proton mass, M_d is the dark mass, M_g is the gas mass, and M_s is the stellar mass contained within a radius r . Axisymmetric solutions will appear in future work.

The most general solution to equation (2) is

$$kT(r) = \frac{\mu m_p}{\rho_g} \left(P_c - \int_{r_c}^r \frac{GM\rho_g}{r'^2} dr' \right) \quad (3)$$

where P_c is the pressure at an arbitrary radius $r = r_c$. The emitted spectrum within any volume then becomes

$$\int n_e n_H \lambda_\nu \left[\frac{\mu m_p}{\rho_g} \left(P_c - \int_{r_c}^r \frac{GM\rho_g}{r'^2} dr' \right), Z \right] dV \quad (4)$$

Thus the spectrum is expressed purely as a function of mass and metallicity. No temperature fitting is required.

Once we know the pressure, the Sunyaev-Zeldovich decrement follows directly from an integral of the pressure along the line of sight (Birkinshaw 1999):

$$y_{SZ} = \int \frac{P\sigma_T}{m_e c^2} dz \quad (5)$$

where σ_T is the electron scattering cross section, and m_e is the electron mass. Similarly, the reduced weak gravitational lensing shear in the tangential direction may be calculated directly from the total mass model (Miralda-Escude 1991):

$$\langle g_T \rangle(R) = \frac{\bar{\kappa}(< R) - \kappa(R)}{1 - \kappa(R)} \quad (6)$$

$$\kappa(R) = \frac{\Sigma(R)}{\Sigma_{\text{crit}}} = \frac{1}{\Sigma_{\text{crit}}} \int_{-\infty}^{\infty} (\rho_d + \rho_g + \rho_s) dz \quad (7)$$

$$\bar{\kappa}(< R) = \frac{2}{\Sigma_{\text{crit}} R^2} \int_0^R R' \Sigma(R') dR' \quad (8)$$

$$\Sigma_{\text{crit}} = \frac{c^2}{4\pi G} \frac{1}{D_A \beta_{\text{WL}}} \quad (9)$$

Here g_T is the reduced tangential shear, κ is the convergence, $\Sigma(R)$ is the surface mass density, D_A is the angular diameter distance to the cluster, and β_{WL} is a measure of the redshift distribution of the lensed sources; see Hoekstra et al. (1998) (§6), and §3.3 below.

2.3. Boundary conditions

The values of P_c and r_c are influenced by the choice of the outer cluster boundary. In the idealized case that the cluster is infinite, P_c and r_c are fixed by the physical requirements that the temperature be everywhere finite and that the gas density decline monotonically with r . Then as $r \rightarrow \infty$, the term in parenthesis must vanish at least as fast as ρ_g ; otherwise, the temperature at large radii will be infinite. Thus

$$P_c = \int_{r_c}^{\infty} \frac{GM\rho_g}{r'^2} dr' \quad (10)$$

and

$$kT(r) = \frac{\mu m_p}{\rho_g} \int_r^{\infty} \frac{GM\rho_g}{r'^2} dr'. \quad (11)$$

Of course, real relaxed clusters are not infinite; at some point, accretion from the surrounding intergalactic medium, and its associated shocks, become important (Ostriker, Bode, & Babul 2005). To simulate this we truncate the cluster at its virial radius. P_c is then the “surface pressure” or pressure of the gas at the outer boundary. Assuming that the density of the intergalactic medium and the ICM at the termination point are the same, a useful estimate of this boundary pressure is

$$P_c = q\rho_g v_{\text{circ}}^2 = q\rho_g \frac{GM_{\text{tot}}}{r_{\text{vir}}} \quad (12)$$

Where r_{vir} is the virial radius (and the radius of termination), v_{circ} is the circular velocity of the halo, and q is a constant of order unity. Both q and v_{circ} are a function of the cosmological parameters. For the prevailing Λ CDM cosmology, $q \sim 1.1$ and $r_{\text{vir}} = r_{100}$, the radius at which the cluster density is 100 times the critical density of the universe (Pierpaoli, Scott, & White 2001).

2.4. Model Radial Profiles

We now require parameterized profiles to insert into the right-hand sides of equations (1) and (3). Because we are eliminating the temperature from the two equations, no assumptions regarding the form of the temperature profile are required. However, we still require parameterized gas, dark, and stellar mass profiles, as well as a metallicity profile.

For the gas profile, we use a “triple” β -model *gas density* profile. Most relaxed clusters of galaxies studied to date have surface brightness distributions that are well-described by a double β -model (Mohr, Mathiesen, & Evrard 1999; Hicks et al. 2002; Lewis et al. 2003; Jia et al. 2004; Johnstone et al. 2005); however certain cases a triple version is required to achieve a good fit (Pointecouteau et al. 2004; Vikhlinin et al. 2006, e.g.).

Our version of the triple β -model is

$$\rho_g = \sum_{i=1}^3 \rho_i (1 + r^2/r_{x,i}^2)^{-3\beta_i/2}, \quad (13)$$

Note that in contrast to previous work, we define the triple β model in density, not in surface brightness. The asymptotic behavior of our triple β model is the same as the behavior of a surface brightness model with the same β parameters; only the details of the transitions among the various regimes are different. While the multiple β model has several more fitting parameters than a broken power law, it is demonstrably better in many cases, e.g. Sun et al. (2004).

For the dark matter distribution, JACO allows for a choice of profiles from the N-body and dynamical literature. A fundamental prediction of most collisionless CDM simulations is that $\rho_{\text{dm}}(r)$ rises inwardly as r^{-1} or steeper to radii comparable within the resolution limit. The resulting model has become known as the “universal” dark matter profile:

$$\rho_U = \rho_0 (r/r_d)^{-n} (1 + r/r_d)^{n-3}, \quad (14)$$

where $x \equiv r/r_d$. Traditionally, $n = 1$ (Navarro et al. 1997) to 1.5 (Moore et al. 1998); however, we explore all values $0 \leq n \leq 2$ to test for softened as well as cuspy dark matter potentials. A similar profile that closely describes the distribution of stars in elliptical galaxies is the “ γ profile” (Dehnen 1993; Tremaine et al. 1994):

$$\rho_\gamma = \rho_0 (r/r_d)^{-n} (1 + r/r_d)^{n-4}. \quad (15)$$

The widely used Hernquist (1990) profile is a special case of the γ profile with $n = 1$. Unlike the universal profiles, the γ family of profiles have simple analytical properties and finite total mass. We also allow for a simple, single power law mass distribution by taking the limit $r_d \rightarrow \infty$ in equation 14.

Finally, the stellar matter distribution in the BCG can be modeled either as a single β -model or as a modified three-dimensional Sérsic (1968) profile:

$$\rho_S = \rho_0 \exp(-(r/r_s)^{\alpha_s}) \quad (16)$$

Thus $\alpha_s = 1/n_s$, where n_s is the Sérsic index such that $n = 4$ gives a de Vaucouleurs (1953) profile. The shape parameters of the this profile are measured from high quality optical photometry, while the normalization is allowed to vary freely in the fit. The BCG profile allows

us to define a constant baryon fraction (f_b) dark matter model—this is a fiducial model where the dark matter density is proportional to the sum of the gas and the BCG stellar densities.

The γ and Sérsic profiles above have closed-form integrated mass profiles. For the others, the enclosed mass can be expressed as a rapidly computable incomplete beta function (see Appendix A).

The radial dependence of the metallicity distribution is not as well constrained by previous studies. We do know that relaxed clusters of galaxies show ample evidence of negative radial metallicity gradients, but the exact form of the decline is not clear. We choose the general distribution

$$Z(r) = \frac{Z_0 r_Z + Z_1 r}{r_Z + r}, \quad (17)$$

i.e., the metallicity progresses smoothly from Z_0 at the center to Z_1 at the outer regions, with a rate controlled by r_Z . This functional form is consistent with the abundance profiles derived from observations (Irwin & Bregman 2001; De Grandi & Molendi 2001; Sun et al. 2003; Buote et al. 2003; de Plaa et al. 2004).

Each radial profile has 3 or more free parameters. The grand total fit to the cluster involves more than a dozen free parameters. Table 1 is an annotated list of all such parameters. Not all parameters need to be fit at the same time; any number can be linked together or frozen at specific values. In most applications, the cluster redshift and the parameters relating to the shape of the stellar light profile will be fixed at specific values, because it is difficult or impossible to estimate them from X-ray data alone. In the case of poor quality data one can restrict the cluster model to a single β -model or to a constant metallicity.

2.5. Projection

Deprojected spectral or temperature data points are always correlated. Use of the χ^2 statistic to fit correlated data is complex, and problematic if the covariance matrix of the deprojected data is unknown. A straightforward alternative is to project the model spectra on the sky, and fit them to the uncorrelated data. For projection we follow the “Smaug” method (Pizzolato et al. 2003) in detail. If the inner and outer edges of the i th annulus are at projected distance R_{i-1} and R_i respectively, then the observed flux is:

$$F_\nu(i) = \frac{1}{4\pi D_L^2} \int_{R_{i-1}}^{R_i} 2\pi R dR \int_R^{r_{\text{max}}} \frac{2\epsilon_{\nu'} r dr}{\sqrt{r^2 - R^2}}, \quad (18)$$

Where $\nu' = \nu/(1+z)$, D_L is the luminosity distance to a source at redshift z , and r_{max} is the outer limit of the cluster. By switching the order of integration, it is possible to further simplify the integral (Pizzolato et al. 2003):¹

$$F_\nu(i) = \frac{1}{D_L^2} \int_{R_{i-1}}^{r_{\text{max}}} r \epsilon_{\nu'} K(r) dr \quad (19)$$

where

$$K(r) = \begin{cases} \sqrt{r^2 - R_{i-1}^2} & \text{if } r < R_i \\ \sqrt{r^2 - R_{i-1}^2} - \sqrt{r^2 - R_i^2} & \text{if } r > R_i \end{cases} \quad (20)$$

¹ Note that Pizzolato et al. (2003) have an extra 4π in front of their equation (3) because they take a different definition of the emissivity.

TABLE 1
LIST OF PARAMETERS IN THE CLUSTER MODEL

Parameter	Sherpa Name	Units	Can be fit?	Comments
Δ	contrast	...	N	Overdensity for masses and concentrations
...	precision	...	N	Precision goal
ρ_d	darkmodel	...	N	Integer specifying dark mass model
ρ_*	starmodel	...	N	Integer specifying stellar mass model
z	redshift	...	Y	Cluster redshift
M_g	Mg	$10^{14} M_\odot$	Y	Gas mass within r_Δ
r_{x1}	rx1	Mpc	Y	Core radius of first β -model
r_{x2}	rx2	Mpc	Y	Core radius of second β -model
r_{x3}	rx3	Mpc	Y	Core radius of third β -model
β_1	b1	...	Y	Slope of first β -model
β_2	b2	...	Y	Slope of second β -model
β_3	b3	...	Y	Slope of third β -model
f_2	xfrac2	...	Y	Normalization of second β -model relative to the 1st
f_3	xfrac3	...	Y	Normalization of third β -model relative to the 1st
M_d	Md	$10^{14} M_\odot$	Y	Dark mass within r_Δ
n	ndark	...	Y	Slope of dark matter density profile
r_0	r0	Mpc	Y	Size of inner constant-density dark matter core
r_d/c	rdm1	...	Y	Dark matter concentration ^a
Z_0	z0	...	Y	Metallicity at $r = 0$
Z_∞	zinf	...	Y	Metallicity at large radii
M_{BCG}	Mstar	$10^{14} M_\odot$	Y	Total stellar mass of BCG
α_s	alpha	...	Y	Index of 3D stellar light profile, $\exp(-(r/rs)^{\alpha_s})$
r_s	rs	Mpc	Y	Scale radius of stellar profile
r_{shock}	rshock	Mpc	Y	Radius of termination shock

NOTE. — Additional parameters representing the residual soft X-ray background may also be fit to the data.

^aThe user can decide to fit the concentration $c \equiv r_\Delta/r_d$, or else to fit r_d itself.

2.6. PSF Distortion

A crucial step in comparing the projected model to the data is to account for PSF distortions. The JACO approach is to manipulate the data as little as possible, so we apply the distortion to the model spectra $F_\nu(i)$ via a convolution matrix:

$$S_\nu(i) = \sum_{j=1}^N \Pi_\nu(i, j) F_\nu(j) \quad (21)$$

where $S_\nu(i)$ is the final model spectrum for comparison with the data, and $\Pi_\nu(i, j)$ contains the energy-dependent contribution of each annulus to itself and every other annulus. Given any set of annuli it is possible to calculate $\Pi_\nu(i, j)$ and thus convolve the model with the PSF.

In general, the PSF of Chandra and XMM-Newton is a function of energy and position. JACO makes an allowance for this. However, the shape of the PSF is not strictly circular or even ellipsoidal. We take no account of this anisotropy, instead treating the PSF as azimuthally symmetric at every point. In-flight XMM-Newton calibration studies have found that this treatment of the PSF yields sufficiently accurate encircled energy profiles except for very bright point sources (Ghizzardi 2001a, 2001b). The model PSF is given by

$$p_\nu(\phi) \propto (1 + \phi^2/\phi_0^2)^\zeta \quad (22)$$

where ϕ is the angular distance in arcseconds between the source center and the position being considered. The shape parameters ϕ_0 and ζ are functions of energy and position across the detector, and are empirically fit as polynomials in photon energy $E = h\nu$ and source position θ :

$$\phi_0 = c_1 + c_2 E + c_3 \theta + c_4 E \theta \quad (23)$$

TABLE 2
ENERGY DEPENDENCE OF THE PSF

Coefficient	ACIS	MOS1	MOS2	pn
c_1	1.137	5.074	4.759	6.636
c_2	-0.054	-0.236	-0.203	-0.305
c_3	0.076	0.002	0.014	-0.175
c_4	0.034	-0.018	-0.023	-0.007
c_5	6.119	1.472	1.411	1.525
c_6	-0.254	-0.010	-0.005	-0.015
c_7	-0.652	-0.001	-0.001	-0.012
c_8	0.051	-0.002	0.000	-0.001

$$\zeta = c_5 + c_6 E + c_7 \theta + c_8 E \theta \quad (24)$$

Here θ is measured in arcminutes and E is measured in keV. The XMM-Newton calibration team has derived (Ghizzardi 2001a, 2001b) values of c_{1-8} from archival observational data. While extensive treatment of the Chandra PSF exists, no functional fits to the azimuthally averaged Chandra PSF have been published. For this reason, we undertake ray-tracing MARX (Wise 1997) simulations of bright point sources at various off-axis angles and energies.

We find that equation (22) provides an acceptable description of the Chandra PSF as well. We measure c_{1-8} in a similar manner to Ghizzardi (2001a), except that we use ray-traced rather than in-orbit data. The polynomial coefficients for all instruments are shown in Table 2.

Using this functional form for the PSF we can calculate the PSF convolution matrix $\Pi_\nu(i, j)$. The details of the calculation are given in Appendix B.

2.7. Software Interface

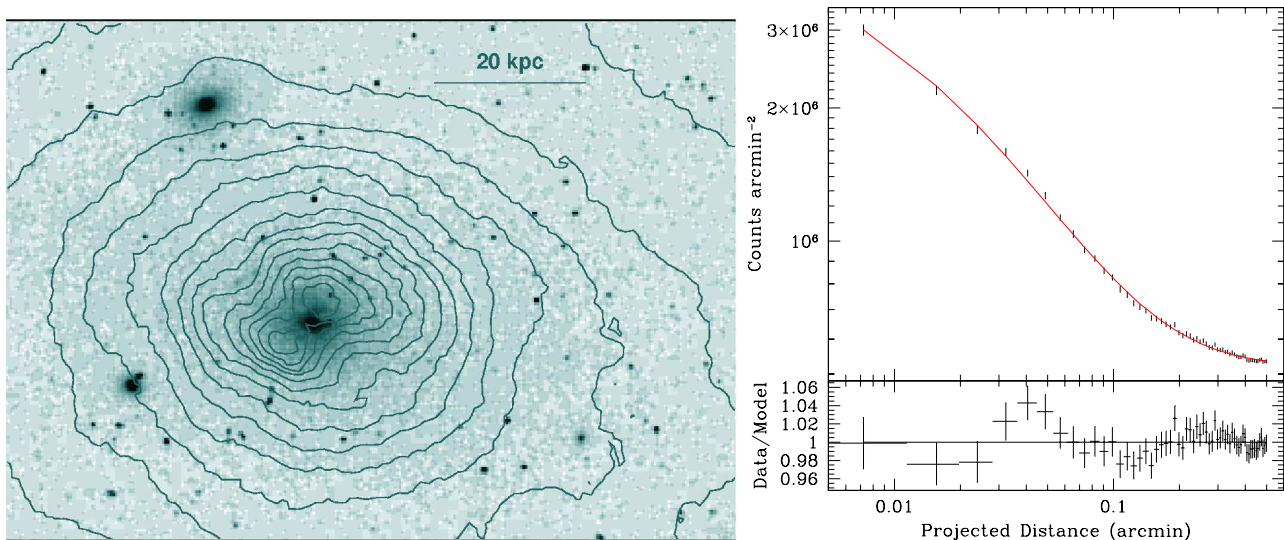


FIG. 1.— (left) HST WFPC2 image of the core of Abell 478, with superposed X-ray contours from the Chandra ACIS-S image. right Profile of the surface brightness plus background for the BCG, as well as the best-fit Sérsic model ($\alpha = 0.289$).

The JACO software package will soon be publicly available at <http://jacocluster.sourceforge.net>. It consists of the following components:

1. A core C language library which calculates the observed X-ray spectrum, tangential shear, and Compton y parameter from the input dark, gas, and stellar mass distributions;
2. An interface which links the core library to the Sherpa data analysis package (Freeman, Doe, & Siemiginowska 2001) as a standard user-defined model, and provides the necessary scripts for graphical viewing and fitting;
3. A parallelized interface, Hrothgar, which runs the core JACO routine on multiprocessor facilities such as Beowulf clusters. Hrothgar is a general purpose package and will soon be available at <http://hrothgar.sourceforge.net>.
4. A set of optional data reduction scripts which process standard archival X-ray data releases according to the procedures described in Appendix C. Weak lensing and SZ data reduction is up to the user. On request, the authors can also provide a routine for transforming JACO Compton y maps into interferometer observables. The existing routines are customized for the Cosmic Background Imager (Padin et al. 2002), but other arrays are easily accommodated.

JACO offers a choice of numerical integration methods. The faster method uses an adaptive Gauss-Legendre quadrature with 10 or 20 abscissae depending on the complexity of the integral. JACO also offers adaptive Gauss-Kronrod quadrature with convergence checking. The latter method is slower but is guaranteed to converge to a given accuracy. We find that the faster method produces model spectra with a median accuracy of 0.1%.

3. APPLICATION TO ABELL 478

Because the JACO technique is new, we apply it to a well-known, relaxed cluster of galaxies. Abell 478 is

a rich cluster at $z=0.088$. The most recent available studies with Chandra (Sanderson et al. 2005; Voigt & Fabian 2006) and XMM-Newton (Pointecouteau et al. 2004) suggest a peak ICM temperature of $\sim 7 - 9$ keV, making this cluster one of the more massive known within $z < 0.1$. For this analysis we assume $H_0 = 70$ km s $^{-1}$ Mpc $^{-1}$, $\Omega_0 = 0.3$, and $\Omega_\Lambda = 0.7$. With these values, $1' = 98.7$ kpc at the distance of Abell 478.

This cluster is an ideal test case for JACO, and highlights the advantages of direct spectral fitting for hydrostatic mass determination. The Chandra and XMM-Newton observations record a total of over 1,000,000 source photons; yet Pointecouteau et al. (2004), Sanderson et al. (2005), and Voigt & Fabian (2006) show that temperature profiles of this cluster disagree when calculated with single temperature emission-weighted plasma. We will show that the addition of optical data (for the stellar mass profile and the weak gravitational lensing shear) and radio data (for the Sunyaev-Zel'dovich decrement) improves the constraints on the dark matter distribution in the cluster, and bring the Chandra and XMM-Newton data into closer agreement.

3.1. X-ray Data

To model Abell 478, we fit JACO X-ray models to available XMM-Newton and Chandra archival. There are four instruments in all: EPIC pn, EPIC MOS 1 and 2, and Chandra ACIS-S. We used XMM-Newton observation sequence 109880101 (126ks, of which 43ks were useful) and Chandra ObsID 1669 (42ks, of which all was useful). For the Chandra data, we use CIAO 3.3 and CALDB 3.2.1. For the XMM-Newton data, we use the latest CCF calibration release before August 2006.

We apply the generic reduction described in Appendix C. We extract spectra in circular regions around the X-ray centroid, which coincides in all datasets with RA(J2000) = 04:13:25.3, DEC(J2000) = +10:27:54. A total of 76 annuli are used, of which Chandra covers only the innermost 40. The ACIS data are used to choose the sizes of the innermost 40 annuli; we require at least 2500 background-subtracted counts per annulus. A similar requirement is used to choose the sizes of the outer 36

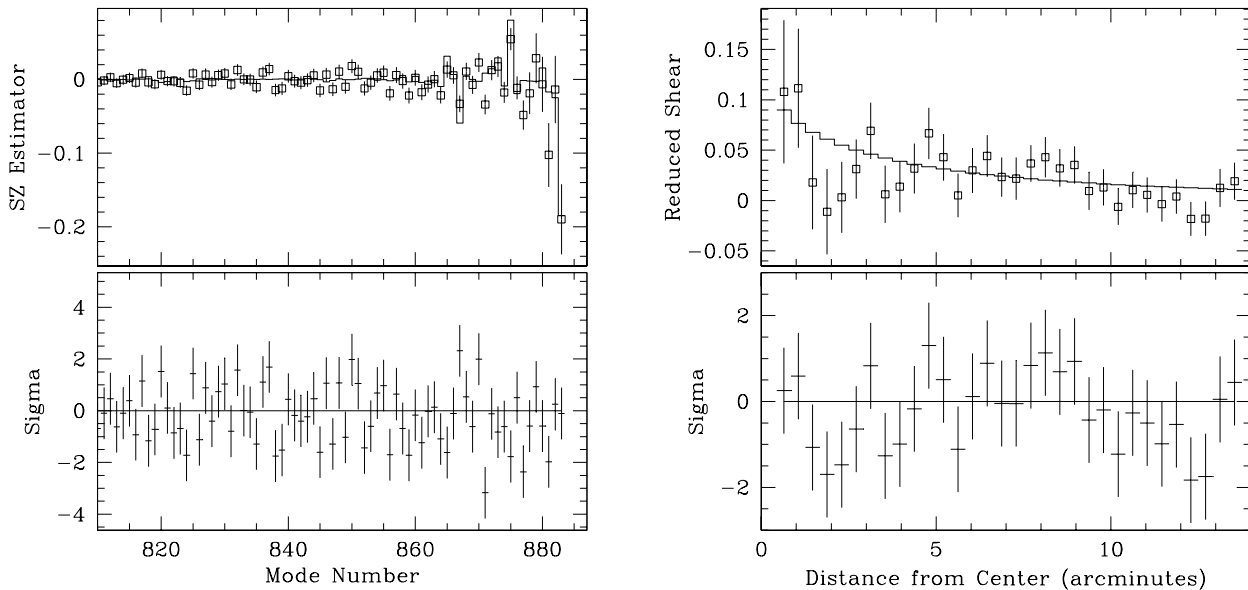


FIG. 2.— (left) SZ data and residuals for the best-fit JACO model; (right) weak lensing data and residuals for the best-fit JACO model

annuli—2500 background-subtracted counts in the EPIC pn camera. The innermost annulus is $13''$ (22 kpc) in radius; the annuli increase regular by $5''$ (8 kpc) until a distance of $4.6'$ (450 kpc), at which point they increase by $14''$ – $40''$ until the final annulus at $9'$ (890 kpc). The extracted spectra were fit over the 0.6–6 keV energy range. The JACO plasma code was set to MEKAL.

The galactic absorption column varies with position on the sky (Sun et al. 2003; Pointecouteau et al. 2004; Vikhlinin et al. 2005). This effect is more important for the XMM-Newton data, which cover a wider field than Chandra; we take the gradient into account by allowing the hydrogen column density to vary linearly with radius. Taking the variation of n_H with position into account still does not resolve the temperature discrepancies between the Chandra and XMM-Newton temperatures at intermediate radii (Pointecouteau et al. 2004; Vikhlinin et al. 2005).

3.2. Hubble Space Telescope Data

Figure 1 shows a 300s archival Hubble Space Telescope WFC2 image of the central ~ 60 kpc diameter region. The corresponding HST observation number is U5A40901R, taken with the $\sim 2000\text{\AA}$ bandpass F606W filter. Superposed are the Chandra ACIS surface brightness contours.

The stellar mass of the BCG makes a non-negligible contribution to the matter distribution within 50 kpc (Sand et al. 2002, 2004; Vikhlinin et al. 2006), and hence contributes to the equation of hydrostatic equilibrium at all radii. To model the stellar mass profile of the BCG, we fit its HST surface brightness profile with a 3D Sérsic (1968) model (equation 16). Figure 1 shows the best fit model: $\alpha_{\text{BCG}} = 0.289 \pm 0.002$ and $r_0 = 0.36 \pm 0.02''$. This model is added to the gaseous and dark components when conducting the grand total fit.

Using the photometric solution for the HST image, we calculate an uncorrected F606W magnitude of 15.1 ± 0.1

by integrating the best-fit Sérsic model to infinity. The galaxy is in a high-extinction region; $E(B-V) = 0.589$ (Schlegel, Finkbeiner, & Davis 1998). After applying the extinction correction of 1.7 mag and a k-correction 0.14 mag (Poggianti 1997), we find that the total F606W luminosity of the galaxy is $4.9 \pm 0.3 \times 10^{11} L_\odot$. This value is important in constraining the average stellar mass-to-light ratio of the BCG, Υ_{BCG}^* . For an evolved stellar population with mean age $\gtrsim 3\text{Gyr}$ in the wavelength regime of the F606W filter, it is expected that $1 < \Upsilon_{\text{BCG}}^* < 4M_\odot/L_\odot$ depending on the stellar initial mass function (IMF) (Maraston 1998). The lower limit of 1 applies regardless of the choice of IMF (Maraston 1998).

3.3. Weak Lensing Data

The weak lensing measurements for A478 are based on archival data taken with the CFH12k camera on the Canada-France-Hawaii-Telescope (CFHT). The camera consists of an array of 6 by 2 CCDs, each 2048 by 4096 pixels. The pixel scale is $0.206''$, which ensures good sampling for the sub-arcsecond imaging data used here. The resulting field of view is about 42 by 28 arcminutes, which is of great importance when studying nearby clusters, such as A478.

The weak lensing analysis requires good image quality and therefore we selected only data with seeing better than $0.8''$. This selection yielded 9 exposures with 605s of integration each, resulting in a total integration time of 5445s. Unfortunately only *R*-band observations were available. This in principle complicates removal of cluster members. However, our study of a large suite of *R*-band observations of other clusters (Hoekstra 2007) has shown that we can readily correct for this source of contamination using the excess galaxy counts as a function of radius.

Detrended data (de-biased and flatfielded) are provided to the community through CADIC. We process this

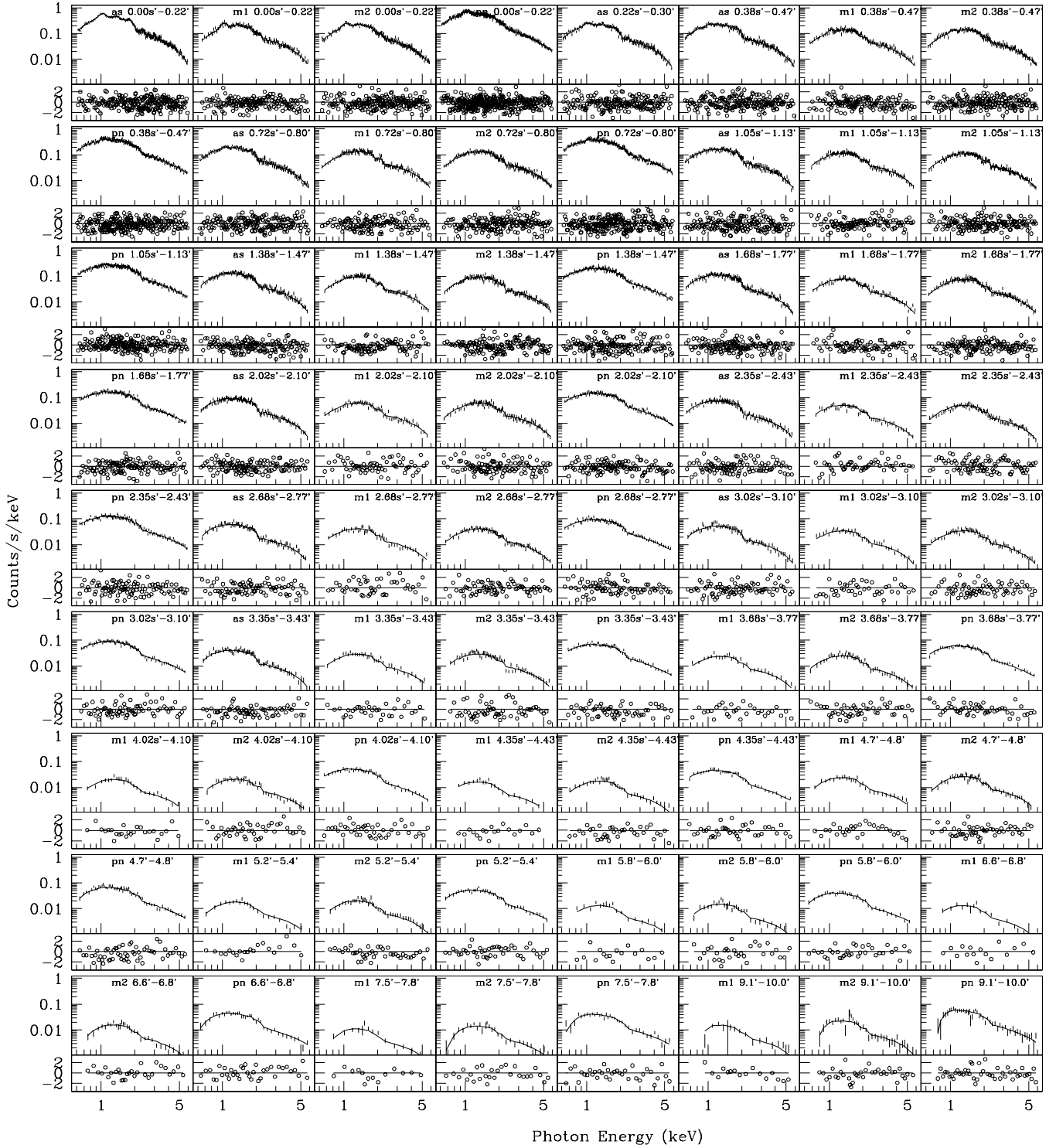


FIG. 3.— Spectra and best-fit models for Chandra ACIS-S (as), XMM-Newton MOS1 (m1), MOS2 (m2), and pn cameras. Only 72 of the 268 total spectra are shown; the inner and outer radii of the extracted annuli (in arcminutes) appear next to the instrument name.

data through the analysis pipeline described in Hoekstra et al. (1998), Hoekstra, Franx, & Kuijken (2000), and Hoekstra (2007). First we use the hierarchical peak finding algorithm from Kaiser, Squires, & Broadhurst (1995) to find objects with a significance $> 5\sigma$ over the local sky. The peak finder gives estimates for the object size, and we reject all objects smaller than the size of the PSF. The remaining objects are analyzed, which yields estimates

for the size, apparent magnitude and shape parameters and their measurement errors. The image is inspected by eye, in order to remove areas that would lead to spurious detections.

To measure the small, lensing induced distortions it is important to accurately correct the shapes for PSF anisotropy, as well as for the diluting effect of seeing. To characterize the spatial variation of the PSF we select a

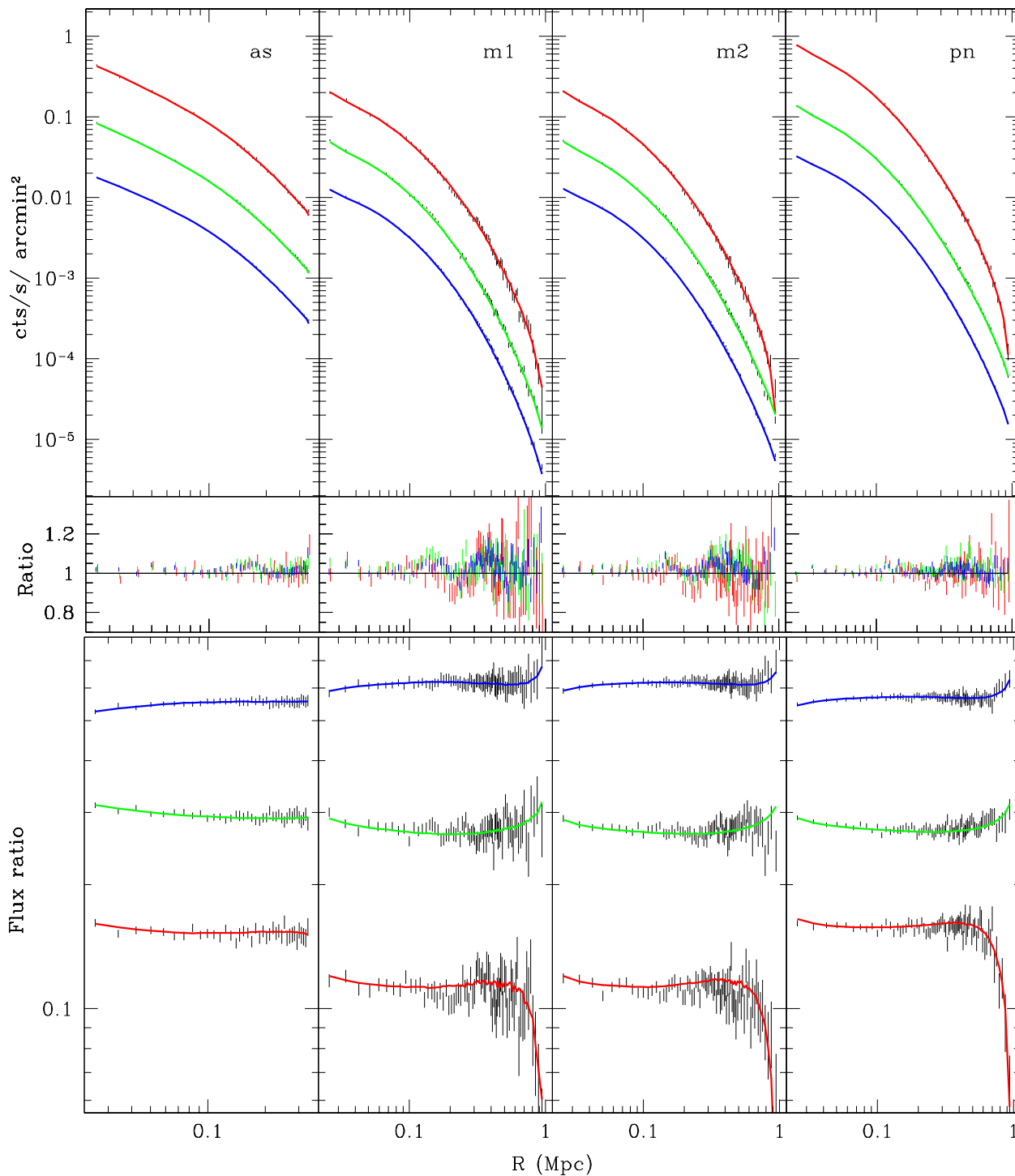


FIG. 4.— Two visualizations of the best-fit universal models (equation 14) for Abell 478. (*top*) The spectra are collapsed into three color regimes: 0.6–1.5 keV (upper line), 1.5–2.0 keV (middle line), and 2.0–6.0 keV (lower line). The count rates are offset 0, -1, and -2 orders of magnitude, respectively, for clarity. Data to model ratios are also shown. (*bottom*) The spectra and models are shown as color ratios. We show the ratio of count rates in the three bands to the total count rate: 0.6–1.5 keV (lower line), 1.5–2.0 keV (middle line), and 2.0–6.0 keV (upper line). Each error bar here represents ~ 50 –70 of the fit spectral data points, each of which in turn represents ~ 50 photons.

sample of moderately bright stars from our images (e.g. Hoekstra et al. 1998). Seeing circularizes the images, thus lowering the raw lensing signal. To correct for the seeing, we need to rescale the polarizations to their “pre-seeing” value, as outlined in Hoekstra et al. (1998). Our pipeline has been tested on simulated images in great detail (e.g. Hoekstra et al. 1998; Heymans et al. 2006). These results suggest that we can recover the shear with

an accuracy of $\sim 2\%$ (Heymans et al. 2006).

The catalog of objects with corrected shapes is used for the weak lensing analysis. In the analysis presented here, we consider the tangential distortion as a function of radius from the cluster center. The resulting measurements, using galaxies with apparent magnitudes $22 < R < 24.5$ are shown in Figure 2.

The interpretation of the lensing signal requires knowl-

edge of the redshifts of the source galaxies. Based on our data alone, we do not know the redshifts of the individual sources. The observed lensing signal, however, is an ensemble average of many different galaxies, each with their own redshift. As a result, it is sufficient to know the source redshift distribution to compute the average value $\beta = \langle D_{ls}/D_s \rangle$. Based on the Hubble Deep Fields, we obtain $\beta = 0.8$. We note that, because A478 is a low redshift cluster, the inferred lensing mass is rather insensitive to the detailed source redshift distribution as effectively all background galaxies are far away.

3.4. Sunyaev-Zel'dovich Data

The SZ data were taken with the Cosmic Background Imager (CBI; Padin et al. 2002) over 11 nights as part of a complete sample of X-ray luminous, low-redshift ($z < 0.1$) clusters. A478 is a remarkably clean cluster, with no apparent point sources at 30 GHz in the CBI data. By far the dominant source of noise in the data is the CMB, which reduces the overall significance of detection from 24.8 sigma, if only thermal noise is considered, to 8.3 sigma. See Udomprasert et al. (2004) for a more complete treatment of observing the SZ effect with the CBI, as well as a more detailed description of the A478 data used here.

To calculate χ^2 from the SZ data, we first run the visibilities through CBIGRIDR, the CBI CMB analysis pipeline (Myers et al. 2003). This compresses them into “2000 gridded estimators”, and calculates the noise and CMB covariances between the estimators, as well as source vectors for source projection if so desired (e.g. Bond, Jaffe, & Knox 1998). This is done once per cluster, before fitting cluster models. During the fit, Compton y maps for models are run through the CBI simulation pipeline to generate predicted visibilities, which are then run through CBIGRIDR to generate the predicted estimators. Let Δ be the estimators, Δ_M be the predicted estimators for the current model, S_{CMB} be the CMB covariance matrix, and N be the noise covariance matrix, then $\chi^2 = (\Delta - \Delta_M)^T (N + S_{CMB})^{-1} (\Delta - \Delta_M)$. Since the noise and the CMB covariance are independent of the cluster model, the inverse need be taken only once. In practice, we rotate into a space in which $N + S_{CMB}$ is diagonal using V , the eigenvectors of $N + S_{CMB}$. Let $\Delta^* \equiv V^T \Delta$, then χ^2 reduces to $\sum (\Delta_i^* - \Delta_{M,i}^*)^2 / \sigma_i^2$ where σ_i^2 is the corresponding eigenvalue of $N + S_{CMB}$. This lets us treat the rotated estimators as independent, uncorrelated measurements of the sky. In practice, it takes a few minutes to calculate the eigenvector rotation, and each χ^2 evaluation (including running the visibility pipeline and CBIGRIDR for estimators) takes ~ 0.5 seconds. The data for the mode numbers which contain most of the cluster signal appear in Figure 2. We do not fit mode numbers < 600 , which are guaranteed not to contain any cluster signal.

3.5. Results

First we fit the JACO models separately to the Chandra and XMM-Newton data. We thereby gain insight into how the differences among the four separate instruments affect the estimated physical parameters. The breakdown for each instrument as well as the number of radial bins appear in Table 3. We show $\sim 25\%$ of

the X-ray spectra along with the best-fit spectral models in Figure 3. We also show collapsed views of all the spectral profiles in Figure 4. The number of radial bins exceeds those in previous mass measurement papers (Pointecouteau et al. 2004; Voigt & Fabian 2006; Vikhlinin et al. 2006) by a factor of ~ 5 . This allows us to constrain the dark mass and gas mass (or surface brightness and temperature) profiles simultaneously, and ensures that we do not miss any relevant details in the spatial distribution of the spectra. The simultaneous fits to the SZ and weak lensing data are shown in Figure 2.

The constraints from the fits appear in Figure 5, where we show 68% and 95% the confidence intervals for some of the chief parameters of interest. All plots assume a universal profile with free inner slope n (equation 14). We show the constraints both with and without the inclusion of the weak lensing and SZ data.

The differences in the calibration among the various four instruments are immediately apparent in the X-ray fits. For example, as is typical of rich, hot clusters, the Chandra data yield a higher average temperature (Kotov & Vikhlinin 2005; Vikhlinin et al. 2005), resulting in a higher dark mass measurement. Also notable is the fact that the errors in the Chandra-derived quantities are larger. Even though the Chandra ACIS-S has the superior spatial resolution, XMM-Newton has the greater sky area, so that the constraints on the shape of the dark profile, and especially on the masses at r_{2500} , are tighter for the XMM-Newton data. This is due to the fact that our outer extraction radius for Chandra (450 kpc) is at about $0.6r_{2500}$; quantities computed outside this radius are extrapolations and therefore subject to greater uncertainty.

It is also clear from Figure 5 that the addition of the lensing and SZ data can help constrain the dark matter parameters significantly. For example, the uncertainty in the dark matter concentration as measured by Chandra is halved through the addition of the lensing and SZ data. We explore the additional power afforded by these types of observations in §4.4 below. Most encouragingly, there is no bias or disagreement whatsoever in the joint fit with the additional data sources—the same physical model can account for the X-ray, SZ, and weak lensing observations at the same time.

Chandra is the instrument for which n is most affected by the addition of the SZ and lensing data. The dark matter slope as measured by Chandra alone ($n < 1$) is consistent with the XMM-Newton value (1.1 ± 0.3). When we add the SZ and lensing data to the Chandra data, the slope ($n = 0.7 \pm 0.4$) is brought into closer agreement with XMM-Newton, in that the low $n = 0$ solution is disfavored.

4. DISCUSSION

4.1. Comparison with Previous X-ray Studies

For the first time, we are able to simultaneously constrain all the parameters of physical interest in the mass fitting process, some of which are listed in Table 3. JACO allows us to calculate the joint probabilities of quantities such as the dark mass, the gas metallicity, and the absorbing hydrogen column density. Determination of the *covariance* of such parameters is a unique property of the method, and cannot be easily be duplicated with previous techniques.

In Table 4 we compare the chief structural properties

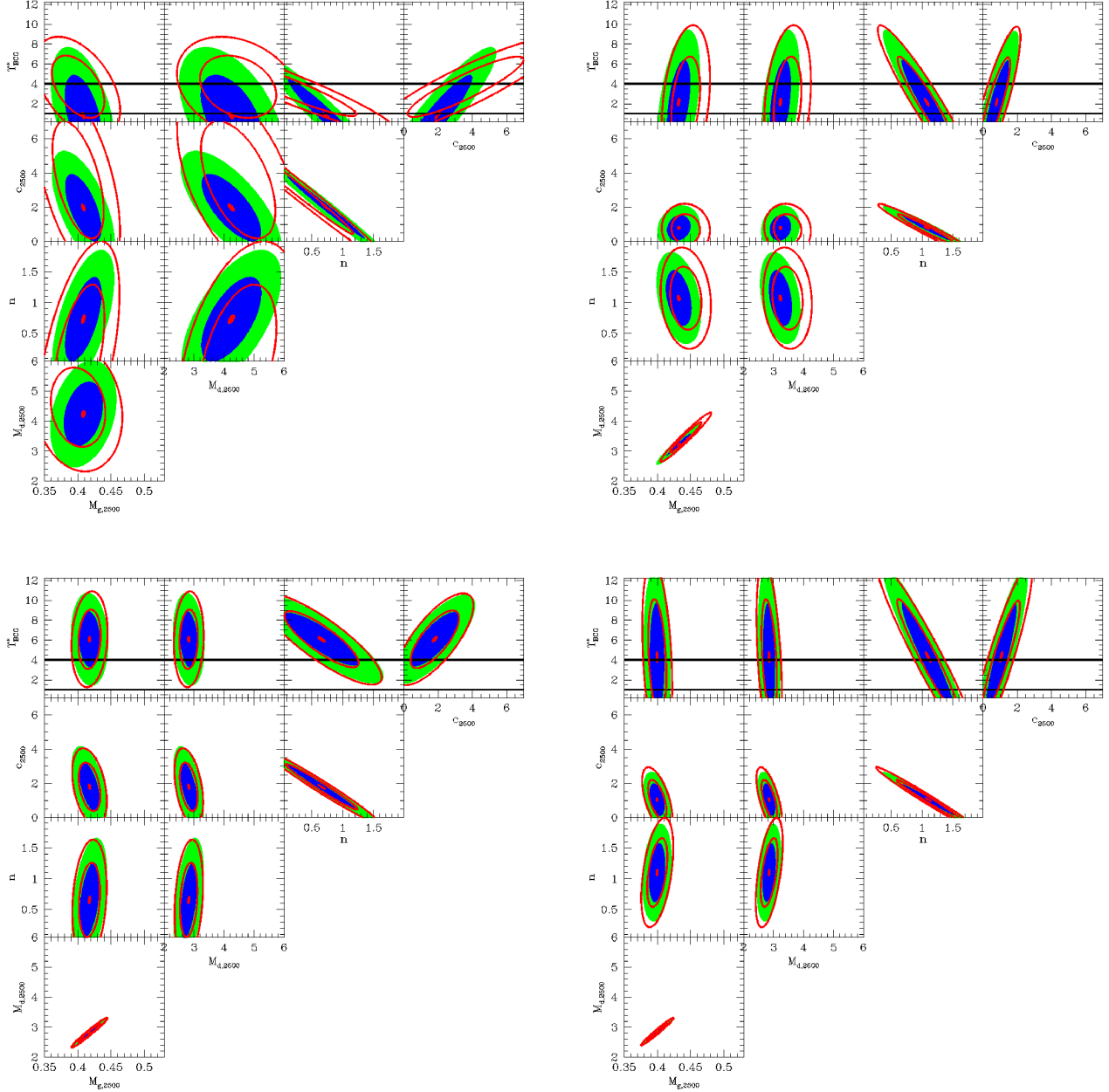


FIG. 5.— 68% and 95% confidence contours on the dark mass within r_{2500} , the gas mass within r_{2500} , the smallest of the three β parameters β_1 , the concentration with respect to r_{500} , the slope of the dark potential n , and the stellar mass-to-light ratio of the BCG Υ_{BCG}^* . All masses are in units of $10^{14} M_{\odot}$. Clockwise from the top left are the Chandra ACIS-S, XMM-Newton MOS1, XMM-Newton pn, and XMM-Newton MOS2 instruments. The filled contours show joint X-ray, SZ, and weak lensing constraints. The unfilled contours show the X-ray constraints alone. The thick lines show the allowed values (from theory) for Υ_{BCG}^* .

of the best-fit JACO model with previous studies of Abell 478. In general, the JACO analysis of the Chandra and XMM-Newton data is in excellent agreement with previous works. In comparing the JACO Chandra results with Sanderson et al. (2005) and Vikhlinin et al. (2006), we note that the uncertainties in the measured JACO parameters are larger. The explanation for this is that JACO allows *all* physical quantities to vary simultaneously during the fitting process. Other fitting techniques conduct a multi-stage fit: first they fix the surface brightness profile at the best-fit multiple β model, and then, using this fixed profile, they fit a temperature profile to the reduced spectra. This results in an underestimate

of the true uncertainties in n and the mass, which are better reflected in the JACO measurements.

We note that the JACO results isolate the dark matter from the gas and stellar profiles. In other studies, the measured n reflects the total gravitational potential. The similarity of the JACO n values compared with the globally measured n in the literature yields the useful conclusion that the stellar and gas profiles do not significantly affect the measured dark matter slopes, at least for Abell 478.

4.2. Contamination by the Central Source

TABLE 3
BEST FIT UNIVERSAL MODELS FOR ABELL 478

	Chandra	EPIC MOS1	EPIC MOS2	EPIC pn	Joint Constraints
X-ray χ^2/DOF	5294/5413 ($q=0.87$)	4170/4084 ($q=0.17$)	6582/6326 ($q=0.012$)	7576/7462 ($q=0.17$)	23264/23345 ($q=0.63$)
Joint χ^2/DOF	5659/5729 ($q=0.74$)	4526/4400 ($q=0.090$)	6936/6642 ($q=0.006$)	7929/7778 ($q=0.11$)	23619/23661 ($q=0.57$)
$M_{g,2500}$	0.403 ± 0.020	0.434 ± 0.013	0.414 ± 0.011	0.399 ± 0.009	0.425 ± 0.007
$M_{d,2500}$	4.273 ± 0.753	3.254 ± 0.263	2.748 ± 0.199	2.839 ± 0.164	3.181 ± 0.135
n	0.709 ± 0.436	1.035 ± 0.312	0.665 ± 0.346	1.096 ± 0.322	1.012 ± 0.207
c_{2500}	2.027 ± 1.270	0.836 ± 0.528	1.966 ± 0.893	1.045 ± 0.633	1.234 ± 0.489
Z_0	0.931 ± 0.153	1.960 ± 0.474	0.731 ± 0.228	1.440 ± 0.718	1.082 ± 0.416
Z_∞	0.095 ± 0.488	0.350 ± 0.144	0.159 ± 0.114	0.443 ± 0.069	0.336 ± 0.065
Υ_{BCG}	< 3	2.573 ± 2.217	5.487 ± 1.829	4.280 ± 3.251	1.669 ± 1.390

NOTE. — Joint constraints on parameters for the Universal fit to each dataset and to the joint data sets, including SZ and weak lensing observations. We also show the goodness of fit q for the X-ray observations alone. For a description of the parameters and their units, see Table 1 and §2.4. The confidence intervals were obtained via the fit covariance matrix.

TABLE 4
COMPARISON WITH PREVIOUS WORK (X-RAY DATA ONLY)

Parameters ^a	JACO Chandra All Data	S05 Chandra All Data	VF06 Chandra All Data	JACO XMM All Data	P05 XMM All Data	JACO Chandra Excised	V06 Chandra Excised	VF06 Chandra Excised	JACO XMM Excised
n^b	< 1	0.35 ± 0.22	0.49 ± 0.45	1.1 ± 0.3	$\equiv 1$	< 1.33	...	$1.1^{+0.2}_{-0.6}$	1.7 ± 0.3
r_{2500}	0.68 ± 0.07	0.62 ± 0.07	$0.76^{+0.67}_{-0.19}$	0.59 ± 0.02	...	0.67 ± 0.07	0.60 ± 0.03
c_{2500}	3.4 ± 2.1	1.1 ± 0.7	...	< 10	< 0.70
$M_{\text{tot},2500}$	4.9 ± 0.9	3.3 ± 0.2	...	4.7 ± 0.8	4.2 ± 0.3	...	3.4 ± 0.3
r_{500}	1.5 ± 0.2	1.4 ± 0.1	...	1.4 ± 0.3	1.4 ± 0.1	...	1.5 ± 0.5
c_{500}	7.4 ± 4.3	2.4 ± 1.3	...	8.6 ± 7.0	3.8 ± 0.3	...	< 2.0
$M_{\text{tot},500}$	9.9 ± 2.6	8.2 ± 1.0	7.6 ± 1.1	9.2 ± 3.8	7.8 ± 1.4	...	11 ± 6
r_{200}	2.2 ± 0.4	2.2 ± 0.1	$3.0^{+14}_{-1.0}$	2.1 ± 0.2	2.1 ± 0.1	2.1 ± 0.3	...	≈ 9.2	2.6 ± 0.6
c_{200}	11 ± 6	7 ± 2	$2.9^{+2.0}_{-2.8}$	3.6 ± 1.7	4.2 ± 0.4	13 ± 9	< 1.2
$M_{\text{tot},200}$	13 ± 4	13 ± 3	...	12 ± 2	11 ± 2	12 ± 3	21 ± 9

NOTE. — Shown are 68% confidence intervals on the structural parameters. JACO: This work; S05: Sanderson et al. (2005); V06: Vikhlinin et al. (2006); VF06: Voigt & Fabian (2006); P05: Pointecouteau et al. (2005). “Chandra” or “XMM” refers to the observatory used by each of the cited works. “All Data” means that no portion of the cluster emission was removed during analysis; “Excised” means that the central $\approx 20 - 30$ kpc was removed before analysis.

^aDistances are in units of Mpc and masses are in units of $10^{14} M_\odot$. In all sources, measurements at r_{500} and r_{200} are based on extrapolation from data within those radii. “Excised” fits exclude the central 30kpc.

^bMeasured for the dark mass profile only in our work, and for the total mass profile in the other papers. All papers assume a universal profile (equation 14) with either free or fixed slope n ; VF06 use a power law of slope n in their excised fit.

A key problem with the mass measurement within the inner 20-30 kpc of Abell 478 (and other similar cool core clusters) is AGN activity. The symmetric bubbles discussed by Sanderson et al. (2005) are clearly visible in Figure 1. All X-ray mass measurement techniques rely on the assumption of hydrostatic equilibrium. However, in most relaxed clusters there is clear, complex interaction between the central AGN/radio source and the intervening gas (e.g. Blanton et al. 2003; Clarke, Blanton, & Sarazin 2004; McNamara et al. 2005).

In the discussion thus far, we have conducted a hydrostatic analysis including this central region. There is at this point no consensus on whether hydrostatic analysis of nonequilibrium gas yields correct results. One common approach (Voigt & Fabian 2006; Vikhlinin et al. 2006) is to excise the inner region from analysis. Note that excising the X-ray emission around the BCG does not mean setting the mass within that region equal to zero—it merely means that the shape of the mass distribution inside that region is not constrained by the X-ray model. For XMM-Newton, excising only the central re-

gion is problematic: the large size of the PSF and the steepness of the surface brightness profile ensure that the central spectrum contributes as far out as $1'$ from the center (Markevitch 2002).

To examine the effects of removing the emission from the disturbed region, we repeat our entire X-ray analysis, excising the central $20''$ (32 kpc) for Chandra, and the central $1'$ (100 kpc) for the XMM-Newton data. The results appear in Table 4. We find that removing the central portion causes us to measure a steeper value for n in both the XMM-Newton and the Chandra data. Outside 100 kpc, the XMM-Newton dark matter profile is consistent with a single power law (the concentration is consistent with 0 in all cases). The Chandra dark profile becomes more fully consistent with an $n = 1$ Universal profile, as first pointed out by Voigt & Fabian (2006).

Given the quality of the Abell 478 observations, these results show that strong constraints on the shape of the dark profile depend greatly on the data within $\approx 20 - 30$ kpc of the center. Unfortunately, we do not yet know whether the hydrostatic model considered here gives cor-

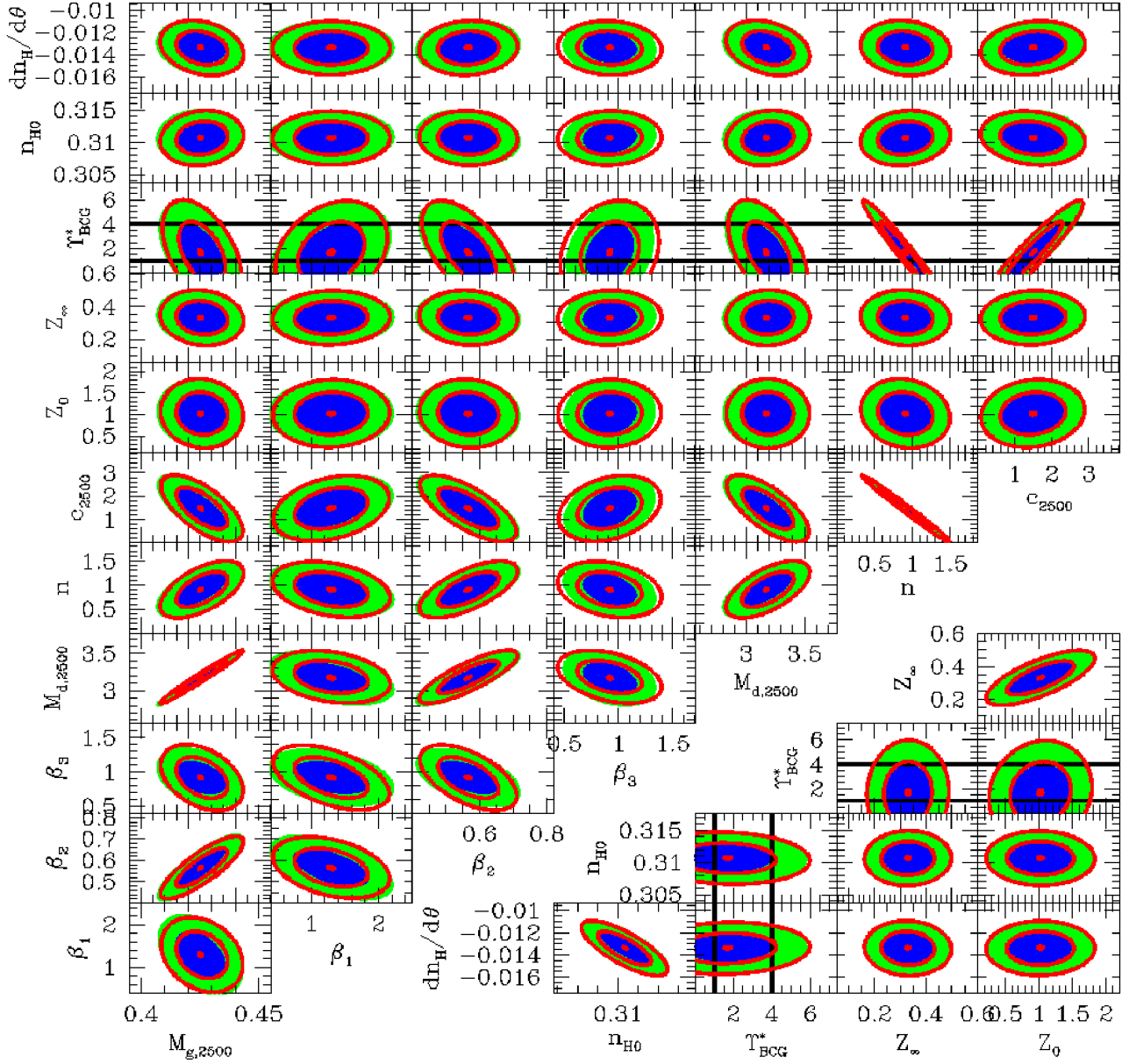


FIG. 6.— 68% and 95% confidence contours for the combined JACO fit to all X-ray, SZ, and weak lensing data. Shown are the dark mass within r_{2500} (in units of $10^{14} M_{\odot}$), the gas mass within r_{2500} , the three β parameters $\beta_{1,2,3}$, the concentration with respect to r_{2500} , the slope of the dark potential n , the metallicity at the core (Z_0) and at large radii (Z_{∞}), the stellar mass-to-light ratio of the BCG Υ_{BCG}^* , the central galactic absorption column n_{H0} in units of 10^{22} cm^{-2} , and its gradient with respect to distance from the center θ in arcminutes. The thick lines show the allowed values (from theory) for the stellar mass-to-light ratio Υ_{BCG}^* .

rect results when applied to regions where AGN heating is important. However, at least for Abell 478, the mass profiles measured for the full data set are consistent with those measured with the central 30 kpc excluded (the latter have larger errors). Thus, treating the central region as hydrostatic does not appear to bias the final measured parameters.

4.3. Combined Constraints from All Data Sources

We now consider the question of conducting a grand total fit to all four instruments. This is a problematic issue, because of the known disagreement in the temper-

ature profiles of this cluster. In combination, the spectra from the four X-ray instruments, together with the lensing and SZ observations, contain 23345 data points (including over a million X-ray photons). To account for the differences in the cross-calibration, the simultaneous fit to all four instruments includes a 4% systematic error added in quadrature to the statistical error. Without the addition of a systematic component no model can simultaneously provide a good fit to both the Chandra and XMM-Newton data. The magnitude of the systematic error was chosen by comparing count ratios in published

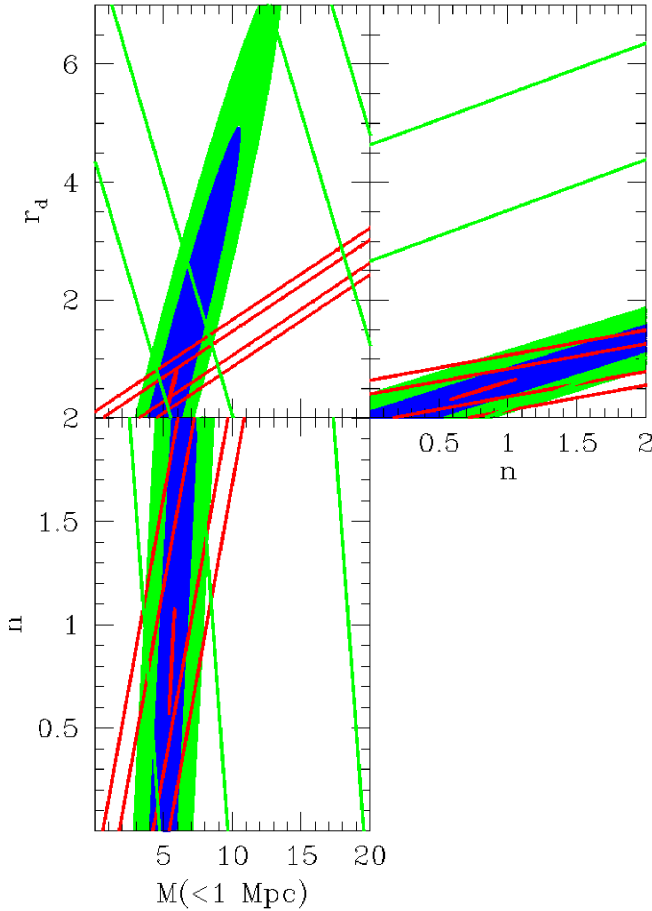


FIG. 7.— Testing the power of the SZ and weak lensing data without gas temperature information. Shown are the dark mass within 1 Mpc in units of $10^{14} M_{\odot}$, the dark radius from equation 14 in units of Mpc, as well as the inner slope n . The X-ray gas mass is taken as a fixed prior, but X-ray temperature (spectral) information is not used. Solid contours show SZ+weak lensing constraints; dark unfilled contours show the lensing constraints alone, and the light unfilled contours show the SZ constraints alone.

cross-calibration studies (Stuhlinger et al. 2006).

Figure 6 shows the combination of all four instruments with the X-ray, SZ, and weak lensing data for the Universal profile. The total number of degrees of freedom are 23661. We find that the $n \sim 1$ universal profile provides the best overall fit, with $\chi^2 = 23619$. The $n \sim 1$ gamma-profile (essentially a Hernquist 1990, profile) provides the next best match, with $\Delta\chi^2 = 15$ with respect to the universal profile. The constant baryon fraction model and the single power law models provide worse matches to the data, with $\Delta\chi^2 = 37$ and $\Delta\chi^2 = 187$, respectively. Using the likelihood ratio test, and noting that a single power law is obtained from the universal profile by setting $r_d = 0$, we estimate that the single power law model is disfavored with false-alarm probability $p < 10^{-6}$.

4.4. The Leverage of SZ and Weak Lensing Data

We showed in §3.5 that the addition of SZ and weak lensing data results in improved constraints on the shape parameters of the gas and dark matter density (at least for the Chandra data taken alone). Here we examine the reasons for this improvement in further detail. As an

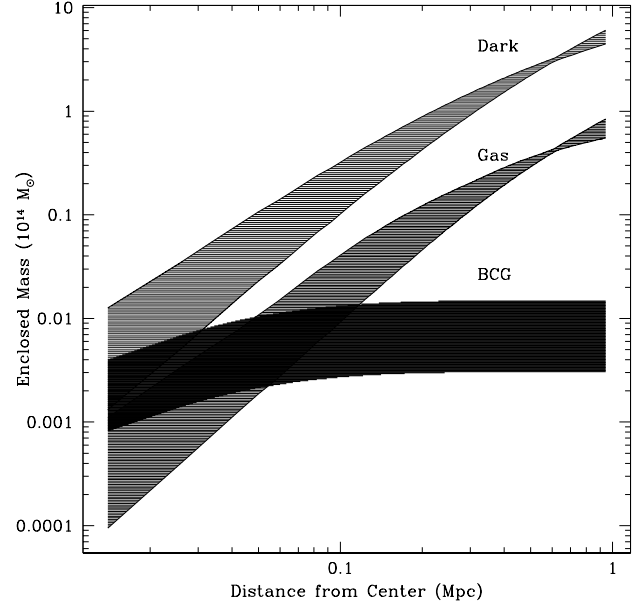


FIG. 8.— Total enclosed mass for the dark, gaseous, and stellar BCG components of Abell 478, in units of $10^{14} M_{\odot}$. Shown are the 68% confidence intervals for fit to all data (Chandra + XMM-Newton + SZ + weak lensing). The stellar mass constraint includes the assumption that the stellar mass-to-light ratio $\Upsilon_{\text{BCG}}^* > 1$.

exercise, we fix the gas mass distribution at the profile derived from the fit to the combined X-ray data. We allow only the dark and stellar mass profiles to vary. Thus we take advantage of the fact that the gas mass profile is a well measured and well agreed-upon quantity for most clusters. For this exercise we ignore the spectral information, where the Chandra and XMM-Newton disagreement is more serious.

The results appear in Figure 7. These figures show that the SZ and weak Lensing data are complementary, as suggested in previous theoretical studies (Zaroubi et al. 2001; Doré et al. 2001). While neither can by itself strongly constrain the slope and concentration of the dark matter profile, together they offer nearly orthogonal constraints on these parameters.

Comparing Figure 7 to Figure 5, it is clear that whenever the quantity of X-ray data overwhelms the SZ and weak lensing data, the statistical weight of the latter two is small; this is why the high quality EPIC pn and MOS2 results are nearly unchanged by the addition of the SZ and weak lensing information. However, when the spatial resolution and the number of X-ray photons is small—as is surely the case for most higher redshift clusters—the SZ and weak lensing information contribute substantially to the constraints on the dark matter profile.

4.5. Dark Matter and the Role of the BCG

The stellar mass of the BCG is an important consideration for modeling the inner regions of galaxy clusters (Lewis et al. 2003; Mamon & Lokas 2005). In Figure 6, the correlation between the dark matter slope n and the stellar mass-to-light ratio Υ_{BCG}^* is strong. The more massive the BCG, the less room there is for a central dark matter cusp. On the other hand, for a given BCG luminosity, there is a minimum value of Υ_{BCG}^* regardless of the stellar initial mass function (IMF). The star light

in effect yields an upper limit on the steepness of the dark matter profile.

A galaxy dominated by a > 3 Gyr old stellar population ought to have $\Upsilon_{\text{BCG}}^* \approx 1 - 4$ in the HST F606W band (Maraston 1998). These limits are shown in Figures 5 and 6. Adopting these limits yields further constraints on the dark matter slope n (towards lower values) and the concentration (towards higher values). For example, in Figure 6, values of $n > 1.1$ would be ruled out by the allowed $\Upsilon_{\text{BCG}}^* = 1$ limit at the 99% confidence level. The ruled-out region changes to $n > 1.3$ if when we use the excised data only. It is worth noting that while the Maraston (1998) population synthesis models have different stellar mass-to-light ratios depending on the exact mixture of stellar populations, only the upper limit ($\Upsilon_{\text{BCG}}^* = 4$) is sensitive to the shape of the initial mass function; the lower limit, $\Upsilon_{\text{BCG}}^* = 1$, is firm and independent of the IMF for a given age.

Figure 8 shows the mass fraction in stars for Abell 478 as a function of distance from the center. As a contributor to the equation of hydrostatic equilibrium, the stars in the BCG are as important or more important than the gas within 80 kpc. The stars also contribute 30% of the total mass within 20 kpc of the center.

5. CONCLUSION

We have developed a new method for measuring the dark matter profile of a cluster directly from X-ray, lensing, and SZ data.

- JACO works directly in the data plane, and generates the observables (X-ray spectra, weak lensing shear profiles, or Sunyaev-Zel'dovich decrement maps) from candidate models. It therefore allows simultaneous constraints on a cluster's dark matter profile using multiwavelength data. It allows joint constraints on all physical parameters of interest.
- JACO explicitly separates the dark, gas, and stellar mass profiles. This allows extraction of the shape of the dark profile independently of the rest of the cluster.
- As long as the gas mass profile is well known, the SZ and weak lensing data together can provide orthogonal constraints on the shape parameters of the dark profile.
- We present new CFHT weak lensing measurements for the well-studied rich cluster Abell 478, and provide an improved reduction of existing CBI Sunyaev-Zel'dovich data. We analyze these data in conjunction with existing Chandra and XMM-Newton observations of the cluster. We find excellent agreement among all data sets when they are fit simultaneously with JACO models. The

weak lensing and SZ observations improve the constraints on the shape of the dark matter distribution from the Chandra data.

- The Chandra and XMM-Newton data for Abell 478 yield similar slopes for the inner dark matter profile: $n < 1$ and $n = 1.1 \pm 0.3$ at the 68% confidence level, respectively. The Chandra constraints become more fully consistent with the $n = 1$ NFW profile when we excise the morphologically disturbed central 30 kpc. A similar result was noted by Voigt & Fabian (2006).
- At intermediate and higher redshifts, where the quality of the X-ray data rapidly diminishes, the SZ and weak lensing data become increasingly important for characterizing the properties of dark matter. In these regimes JACO will be a powerful tool for improving constraints on the shape of the cluster potential.
- JACO as described in this paper will soon be available for public download at <http://jacocluster.sourceforge.net>.

In future papers in this series, we will test JACO against gasdynamical N-body simulations, generalize the method to the axisymmetric case, and use JACO to analyze multiwavelength data for a large cluster sample.

We are grateful for comments from the referee, who led us to improve the paper. We thank Alexey Vikhlinin, Trevor Ponman, George Lake, and Dick Bond for insightful discussions. AM acknowledges partial support from a Chandra Postdoctoral Fellowship issued by the Chandra X-ray Observatory Center, which is operated by the Smithsonian Astrophysical Observatory for and on behalf of NASA under contract NAS 8-39073. AB and HH acknowledge NSERC Discovery Grants. HH acknowledges support from the Canadian Institute for Advanced Research. We acknowledge use of equipment acquired using grants from the Canada Foundation for Innovation and the British Columbia Knowledge and Development Fund. This research used the facilities of the Canadian Astronomy Data Centre operated by the National Research Council of Canada with the support of the Canadian Space Agency. This work is based on observations obtained at the Canada-France-Hawaii Telescope (CFHT) which is operated by the National Research Council of Canada, the Institut National des Sciences de l'Univers of the Centre National de la Recherche Scientifique of France, and the University of Hawaii. This work makes substantial use of version 1.7 of the GNU Scientific Library, an excellent library of numerical routines in C distributed under the GNU General Public License.

APPENDIX

A. FAST EVALUATION OF BROKEN POWER LAW INTEGRALS

To calculate the integrated mass of the profiles considered in §2.4, we often need to calculate integrals of the type

$$M(r) = \int_0^r 4\pi r^2 \rho(r/r_t) dr = 4\pi r_t^3 \rho_0 \int_0^{r/r_t} x^{2-n} (1+x^p)^{\frac{n-q}{p}} dx \quad (\text{A1})$$

where r_t is the characteristic radius of the density ρ , and n and q are the slopes at $r = 0$ and $r = \infty$, respectively. Rather than resorting to hypergeometric functions to evaluate the integral, we can express it in terms of the incomplete beta function $B_y(a, b)$ for which very fast numerical routines exist:

$$M(r) = 4\pi r_t^3 \rho_0 B_y \left(\frac{3-n}{p}, \frac{q-3}{p} \right); y \equiv \frac{r^p}{r_t^p + r^p} \quad (\text{A2})$$

In the common definition of the incomplete beta function, a and b must be positive definite. However, $q-3$ could well be negative (e.g., for a β -model). The following recurrence relations allow us to transform the $2 < q < 3$ cases into incomplete beta functions with positive definite arguments:

$$B_y(a, b) = B(b, a) - B_{1-y}(b, a) \quad (\text{A3})$$

$$B_y(a+1, b) = \frac{1}{a+b} [aB_y(a, b) - (1-y)^b y^a] \quad (\text{A4})$$

where $B(a, b) = B_0(a, b)$ is the complete beta function. For $y < (a+1)/(a+b+2)$, $B_y(a, b)$ is evaluated using rapidly converging continued fractions. For $y > (a+1)/(a+b+2)$, equation (A3) is used to transform the problem back into a regime where the continued fractions converge quickly.

For the specific case that $b = 0$ (e.g. NFW profiles), the transformations cannot be used. However, the continued fraction method yields results accurate to better than 10^{-6} for all interesting values of y so long as a is limited to physically plausible values (i.e. is limited to 1 to 3, corresponding $n = 0$ to 2).

B. CALCULATION OF THE PSF COEFFICIENTS

Here we discuss the approximations used for calculating the scattering of light from an annulus with inner and outer radii (R_{j-1}, R_j) into an annulus with inner and outer radii (R_{i-1}, R_i) . The general expression for $C_\nu(x, y)$, the counts observed using a detector with a monochromatic point spread function $p_\nu(x, y, x', y')$ observing a monochromatic source with flux distribution $I_\nu(x, y)$ is

$$C_\nu(x, y) = \int \int I_\nu(x', y') p_\nu(x, y, x', y') dx' dy' \quad (\text{B1})$$

Approximating the source and the PSF as azimuthally symmetric, the above expression becomes

$$C_\nu(R) = \int_0^{2\pi} \int_0^\infty R' I_\nu(R') p_\nu(R, R^2 + R'^2 - 2RR' \cos \phi) dR' d\phi, \quad (\text{B2})$$

where $R^2 + R'^2 - 2RR' \cos \phi$ is the square of the distance between (x, y) and (x', y') in polar coordinates. Splitting up the source flux $I(R')$ into N homogeneous annuli, we have

$$C_\nu(R) = \sum_{j=1}^N I_\nu(R_{j-1}, R_j) \int_0^{2\pi} \int_{R_{j-1}}^{R_j} R' I(R') p_\nu(R, R^2 + R'^2 - 2RR' \cos \phi) dR' d\phi \quad (\text{B3})$$

where $R \equiv (R_{i-1} + R_i)/2$. Each set of N double integrals yields the PSF correction coefficients at energy $h\nu$. We evaluate the double integral for four photon energies ($h\nu = 0.37, 0.75, 1.5, 3.6$ keV), and interpolate to obtain the correction at arbitrary energy.

C. TECHNICAL DETAILS OF THE REDUCTION AND ANALYSIS

JACO v1.0 includes scripts which prepare the raw data from the Chandra and XMM-Newton archives for analysis. These preprocessing scripts yield a uniformly reduced set of spectra for an entire cluster with minimal human interaction. The use of these scripts is not required for undertaking the JACO analysis. Observers may undertake any reduction procedure in preparation for JACO, subject to the following requirements on the final output spectra:

1. Each spectrum must be extracted from a circular annulus surrounding the cluster center. Future versions of JACO will also handle elliptical annuli.
2. The spectrum keyword BACKSCAL must be set to the net source area in square arcminutes (i.e. excluding the area of any excised regions intersecting the annulus).
3. The redistribution matrix file (RMF) and ancillary response file (ARF) must have the same energy binning for all spectra. The largest bin size that preserves relevant calibration features should be used.

C.1. Pipeline reprocessing

To begin, the JACO preprocessing scripts reapply the latest version of the standard pipeline analysis to the raw data. For Chandra, this has the effect of correcting for the spatial gradients in the filter contamination. For ACIS front-illuminated chips with the appropriate detector temperature, we include the charge transfer inefficiency correction (CTI) (Townsend et al. 2000). For XMM-Newton, we rerun the standard pipeline to include the necessary files for correcting the EPIC pn spectra for the out-of-time (OOT) events.

C.2. Point source removal

Because we are interested only in the diffuse X-ray emitting medium, we remove contaminating point sources from the data. The CIAO wavelet source detection algorithm yields source lists for both the Chandra and the XMM-Newton total band images. Visual inspection and correction of the source lists is necessary to remove spurious detections along chip borders. For each detected point source, we remove an elliptical region with major axis equal to three times the PSF width from photon event files. The source detection program specifies the orientation and axis ratio of the ellipses.

C.3. Flaring background

Flares in the X-ray background can contaminate the spectra and must therefore be screened using the field total light curve at energies $\gtrsim 10$ keV. In many XMM-Newton observations, a substantial fraction of the telescope live time is affected by flares. To screen the XMM-Newton data, we apply 2σ clipping of the light curve binned in 100s intervals. Then we apply the technique of Nevalainen, Markevitch, & Lumb (2005). They find that small flares significantly affect the σ -clipped XMM-Newton data, and that these flares are best filtered by accepting only periods with count rates less than 120% of the mean σ -clipped count rate. For Chandra data, we follow the flare rejection method provided as a standard contributed background analysis package (Markevitch 2005).

C.4. Quiescent particle background

Two types of background affect Chandra and XMM-Newton observations of diffuse sources. The non X-ray particle background is dominated by the interaction of charged and non-charged particles with the CCD. In both observatories, the particle background comprises a continuum as well as spectral line features whose location depends on the particular instrument. Being non X-ray in origin, the particle background is not vignetted—i.e., it is not affected by the variations in the effective area across the CCD. To subtract this background from the spectra, we use the latest public versions of the blank sky observations for XMM-Newton (Read & Ponman 2003) and Chandra (Markevitch 2005). The subtraction is made possible by the fact that after flare rejection, there is little change in the spectral shape of the particle background with position or time; only the normalization varies appreciably.

To carry out the subtraction, we subject the XMM-Newton blank sky spectra to same flare rejection algorithm as the cluster spectra (the Chandra blank sky are already calibrated in the same manner as the observations). We normalize the spectra of the blank sky fields to match the spectra of the cluster fields observed in the 10-12 keV (XMM-Newton) and 8-10 keV (Chandra) energy range (where the effective area for X-ray photons is low). For the purposes of calculating the renormalization factor, we exclude emission from the central 100 kpc of the cluster. For each extracted cluster spectrum, we use the blank sky fields to extract a matching particle background spectrum.

C.5. Residual X-ray Background

Once point sources are removed, the remaining diffuse emission consists of two components: unresolved extragalactic AGN (with index ~ 1.4 power law spectra) and unabsorbed, thermal ~ 0.2 keV background with approximately solar abundance (Markevitch et al. 2003). Unlike the particle background, the soft X-ray background varies with position on the sky, so that it cannot be corrected using blank sky fields.

One option for dealing with the residual background is to ignore it completely by cutting all emission below 1 keV. However, this also removes a significant portion of the cluster signal, including potentially important low-energy line emission. Another option is to measure the spectrum in a source-free region and subtract it from the cluster (Read & Ponman 2003). However clusters of galaxies often fill the entire field of view of the X-ray detector; it is difficult to find a truly source-free region.

Our approach is to model the residual background as part of the fitting process (e.g. Mahdavi et al. 2005). This is the only realistic option when the cluster fills the entire field of view. For each instrument, we add a different unabsorbed thermal plasma with free temperature and abundance and arbitrary (negative or positive) normalization. To account for the diffuse extragalactic background, we add an absorbed power law with slope fixed to 1.4 and similarly free normalization. We require the temperature and metal abundance to be the same for all instruments. However, different normalizations are required for each detector because the instrumental background from the blank sky fields is different for each instrument. When the renormalized instrumental background is subtracted, the net (positive or negative) cosmic background in each field will be different, even though the true cosmic background is the same.

C.6. Spectrum Extraction

At present the JACO method includes only spherically symmetric analysis; we therefore extract spectra in concentric annuli around the cluster center. The cluster center is determined using the peak of the Chandra X-ray emission, and verified using Hubble Space Telescope archival data.

JACO requires a minimum annulus width of $5''$. At these widths, the PSF correction (§2.6) becomes important even for Chandra data. The widths are by default set to be the same for all the instruments considered. The JACO user can set the minimum number of background-subtracted counts required per annulus. The background measured at this stage (and this stage only) is roughly estimated from the region outside the largest circular annulus that will completely fit in the instruments' field of view. The spectra are grouped by default at 40 events per bin, but the user can modify this.

To model the spectra, an accurate knowledge of the total solid angle subtended by each annulus is necessary. Because an annulus can intersect chip gaps, bad pixels, and excised sources, the calculation of this area is not trivial. In particular, the XMM-Newton SAS `backscale` procedure cannot calculate accurate areas for the annuli with the smallest (5'') width. For this reason, JACO creates its own high resolution bad pixel map for each of the three EPIC instruments, and uses it to determine the correct solid angles.

We use the appropriate CIAO and SAS tasks to create response matrices for the spectra. For Chandra, we use `mkwarf/mkacisrmf`; for XMM-Newton, we use `arfgen/rmgfen`. The response functions are emission-weighted through the use of weight maps. Arnaud et al. (2001) argue that this technique is imperfect, because the spatial variation of the uncalibrated source can yield biases in the X-ray temperatures. Their solution, `evigweight`, is an alternative technique for the reduction of XMM-Newton spectra. In `evigweight` the individual photon events are weighted by the inverse of the effective area at the photons' recorded positions, and only one central ARF is created for the entire cluster. Because CIAO does not offer a similar procedure for Chandra spectra, we have compared XMM-Newton spectra derived using the standard method with spectra derived using `evigweight`. We find that for the fine binning used by JACO, the difference between the standard and `evigweight` spectra are negligible as long as the detector map is extracted for energies where the raw counts spectrum is closest to constant, specifically the channels corresponding to the 0.8-1.4 keV photon energy range.

C.7. Covariant Error Analysis: the Hrothgar Parallel Minimizer

The command-line (as opposed to the Sherpa-based) frontend to JACO allows the global χ^2 to be minimized within a clustered computing environment. In essence, Hrothgar runs the Levenberg-Marquard (LM) minimization algorithm (Press et al. 1992) as implemented by the GNU Scientific Library (GSL; <http://www.gnu.org/software/gsl/>). The LM algorithm requires knowledge of the Jacobian of the function to be minimized, which is not analytic for X-ray spectra due to the highly nonlinear nature of the cooling function. Hrothgar calculates the Jacobian numerically using the methods described in Press et al. (1992), with error control as implemented by the GSL library. Because calculation of the Jacobian matrix J during the minimization phase requires $2m$ evaluations of the JACO model for m free parameters, each function evaluation can be assigned to a cluster node, resulting in a speed increase directly proportional to the number of CPUs, up to $2m$ CPUs.

We carry out the error analysis by calculating the covariance matrix $C = (JJ^T)^{-1}$. When computing J numerically for this purpose, we use both the 3-point and the 5-point numerical differentiation rules. The difference between the 3- and the 5-point rules yields an estimate of the error, which we minimize as a function of the step size. The covariance matrix obtained in this manner records the interdependence of all the physical parameters in the JACO analysis. The confidence contours are plotted by the methods described in Press et al. (1992).

Hrothgar will soon be freely downloadable at <http://hrothgar.sourceforge.net>.

REFERENCES

- Ahn, K. & Shapiro, P. R. 2005, MNRAS, 363, 1092
 Allen, S. W., Schmidt, R. W., & Fabian, A. C. 2002, MNRAS, 335, 256
 Arabadji, J. S., Bautz, M. W., & Garmire, G. P. 2002, ApJ, 572, 66
 Arnaud, M., Neumann, D. M., Aghanim, N., Gastaud, R., Majerowicz, S., & Hughes, J. P. 2001, A&A, 365, L80
 Balberg, S., Shapiro, S. L., & Inagaki, S. 2002, ApJ, 568, 475
 Bialek, J. J., Evrard, A. E., & Mohr, J. J. 2002, ApJ, 578, L9
 Birkinshaw, M. 1999, Phys. Rep., 310, 97
 Blanton, E. L., Gregg, M. D., Helfand, D. J., Becker, R. H., & White, R. L. 2003, AJ, 125, 1635
 Bond, J. R., Jaffe, A. H., & Knox, L. 1998, Phys. Rev. D, 57, 2117
 Buote, D. A., Humphrey, P. J., & Stocke, J. T. 2005, ApJ, 630, 750
 Buote, D. A. & Lewis, A. D. 2004, ApJ, 604, 116
 Buote, D. A., Lewis, A. D., Brighenti, F., & Mathews, W. G. 2003, ApJ, 595, 151
 Burkert, A. 2000, ApJ, 534, L143
 Clarke, T. E., Blanton, E. L., & Sarazin, C. L. 2004, ApJ, 616, 178
 De Filippis, E., Sereno, M., Bautz, M. W., & Longo, G. 2005, ApJ, 625, 108
 De Grandi, S. & Molendi, S. 2001, ApJ, 551, 153
 de Plaa, J., Kaastra, J. S., Tamura, T., Pointecouteau, E., Mendez, M., & Peterson, J. R. 2004, A&A, 423, 49
 de Vaucouleurs, G. 1953, MNRAS, 113, 134
 Dehnen, W. 1993, MNRAS, 265, 250
 Doré, O., Bouchet, F. R., Mellier, Y., & Teyssier, R. 2001, A&A, 375, 14
 Dupke, R. & White, R. E. 2003, ApJ, 583, L13
 Ettori, S., Fabian, A. C., Allen, S. W., & Johnstone, R. M. 2002, MNRAS, 331, 635
 Fabian, A. C., Mushotzky, R. F., Nulsen, P. E. J., & Peterson, J. R. 2001, MNRAS, 321, L20
 Fabian, A. C., Sanders, J. S., Allen, S. W., Crawford, C. S., Iwasawa, K., Johnstone, R. M., Schmidt, R. W., & Taylor, G. B. 2003, MNRAS, 344, L43
 Freeman, P. E., Doe, S., & Siemiginowska, A. 2001, in ASP Conf. Ser. 238: Astronomical Data Analysis Software and Systems X, 483+
 Fujita, Y., Sarazin, C. L., Reiprich, T. H., Andernach, H., Ehle, M., Murgia, M., Rudnick, L., & Slee, O. B. 2004, ApJ, 616, 157
 Fukazawa, Y., Botoya-Nones, J. G., Pu, J., Ohto, A., & Kawano, N. 2006, ApJ, 636, 698
 Fukushima, T. & Makino, J. 2001, ApJ, 557, 533
 Gavazzi, R. 2005, A&A, 443, 793
 Ghigna, S., Moore, B., Governato, F., Lake, G., Quinn, T., & Stadel, J. 2000, ApJ, 544, 616
 Ghizzardi, S. 2001a, In Flight Calibration of the PSF for the MOS1 and MOS2 Cameras, Tech. Rep. XMM-SOC-CAL-TN-0022, XMM-Newton Science Operations Center
 —. 2001b, In Flight Calibration of the PSF for the MOS1 and MOS2 Cameras, Tech. Rep. XMM-SOC-CAL-TN-0022, XMM-Newton Science Operations Center
 Grevesse, N. & Sauval, A. J. 1998, Space Science Reviews, 85, 161
 Hallman, E. J. & Markevitch, M. 2004, ApJ, 610, L81
 Hernquist, L. 1990, ApJ, 356, 359
 Heymans, C., Van Waerbeke, L., Bacon, D., Berge, J., Bernstein, G., Bertin, E., Bridle, S., Brown, M. L., et al. 2006, MNRAS, 368, 1323
 Hicks, A. K., Wise, M. W., Houck, J. C., & Canizares, C. R. 2002, ApJ, 580, 763
 Hoekstra, H. 2007, in preparation
 Hoekstra, H., Franx, M., & Kuijken, K. 2000, ApJ, 532, 88
 Hoekstra, H., Franx, M., Kuijken, K., & Squires, G. 1998, ApJ, 504, 636

- Humphrey, P. J., Buote, D. A., Gastaldello, F., Zappacosta, L., Bullock, J. S., Brighenti, F., & Mathews, W. G. 2006, *ApJ*, 646, 899
- Irwin, J. A. & Bregman, J. N. 2001, *ApJ*, 546, 150
- Jia, S. M., Chen, Y., Lu, F. J., Chen, L., & Xiang, F. 2004, *A&A*, 423, 65
- Johnstone, R. M., Fabian, A. C., Morris, R. G., & Taylor, G. B. 2005, *MNRAS*, 356, 237
- Kaastra, J. S., Tamura, T., Peterson, J. R., Bleeker, J. A. M., Ferrigno, C., Kahn, S. M., Paerels, F. B. S., Piffaretti, R., et al. 2004, *A&A*, 413, 415
- Kaiser, N., Squires, G., & Broadhurst, T. 1995, *ApJ*, 449, 460
- Kochanek, C. S. & White, M. 2000, *ApJ*, 543, 514
- Kotov, O. & Vikhlinin, A. 2005, *ApJ*, 633, 781
- LaRoque, S. J., Bonamente, M., Carlstrom, J. E., Joy, M. K., Nagai, D., Reese, E. D., & Dawson, K. S. 2006, *ApJ*, 652, 917
- Lewis, A. D., Buote, D. A., & Stocke, J. T. 2003, *ApJ*, 586, 135
- Mahdavi, A., Finoguenov, A., Böhringer, H., Geller, M. J., & Henry, J. P. 2005, *ApJ*, 622, 187
- Mamon, G. A. & Lokas, E. L. 2005, *MNRAS*, 362, 95
- Maraston, C. 1998, *MNRAS*, 300, 872
- Markevitch, M. 2002, *ArXiv Astrophysics e-prints*, astro-ph/020533
- . 2005, *ACIS Background Cookbook*, Tech. Rep. <http://cxc.harvard.edu/contrib/maxim/acisbg>, Smithsonian Astrophysical Observatory
- Markevitch, M., Bautz, M. W., Biller, B., Butt, Y., Edgar, R., Gaetz, T., Garmire, G., Grant, C. E., et al. 2003, *ApJ*, 583, 70
- Markevitch, M., Gonzalez, A. H., David, L., Vikhlinin, A., Murray, S., Forman, W., Jones, C., & Tucker, W. 2002, *ApJ*, 567, L27
- Markevitch, M. & Vikhlinin, A. 1997, *ApJ*, 491, 467
- . 2001, *ApJ*, 563, 95
- Matsushita, K., Belsole, E., Finoguenov, A., & Böhringer, H. 2002, *A&A*, 386, 77
- Mazzotta, P., Rasia, E., Moscardini, L., & Tormen, G. 2004, *MNRAS*, 354, 10
- McNamara, B. R., Nulsen, P. E. J., Wise, M. W., Rafferty, D. A., Carilli, C., Sarazin, C. L., & Blanton, E. L. 2005, *Nature*, 433, 45
- Merritt, D., Navarro, J. F., Ludlow, A., & Jenkins, A. 2005, *ApJ*, 624, L85
- Miralda-Escude, J. 1991, *ApJ*, 380, 1
- Miralda-Escude, J. & Babul, A. 1995, *ApJ*, 449, 18
- Mohr, J. J., Mathiesen, B., & Evrard, A. E. 1999, *ApJ*, 517, 627
- Moore, B., Governato, F., Quinn, T., Stadel, J., & Lake, G. 1998, *ApJ*, 499, L5
- Myers, S. T., Contaldi, C. R., Bond, J. R., Pen, U.-L., Pogossyan, D., Prunet, S., Sievers, J. L., Mason, B. S., et al. 2003, *ApJ*, 591, 575
- Navarro, J. F., Frenk, C. S., & White, S. D. M. 1997, *ApJ*, 490, 493
- Nevalainen, J., Markevitch, M., & Lumb, D. 2005, *ApJ*, 629, 172
- Ostriker, J. P., Bode, P., & Babul, A. 2005, *ApJ*, 634, 964
- Padin, S., Shepherd, M. C., Cartwright, J. K., Keeney, R. G., Mason, B. S., Pearson, T. J., Readhead, A. C. S., Schaal, W. A., et al. 2002, *PASP*, 114, 83
- Peterson, J. R., Kahn, S. M., Paerels, F. B. S., Kaastra, J. S., Tamura, T., Bleeker, J. A. M., Ferrigno, C., & Jernigan, J. G. 2003, *ApJ*, 590, 207
- Pierpaoli, E., Scott, D., & White, M. 2001, *MNRAS*, 325, 77
- Pizzolato, F., Molendi, S., Ghizzardi, S., & De Grandi, S. 2003, *ApJ*, 592, 62
- Poggianti, B. M. 1997, *A&AS*, 122, 399
- Pointecouteau, E., Arnaud, M., Kaastra, J., & de Plaa, J. 2004, *A&A*, 423, 33
- Pointecouteau, E., Arnaud, M., & Pratt, G. W. 2005, *A&A*, 435, 1
- Poole, G. B., Fardal, M. A., Babul, A., McCarthy, I. G., Quinn, T., & Wadsley, J. 2006, *MNRAS*, 373, 881
- Press, W. H., Teukolsky, S. A., Vetterling, W. T., & Flannery, B. P. 1992, *Numerical recipes in FORTRAN. The art of scientific computing* (Cambridge: University Press, —c1992, 2nd ed.)
- Rasia, E., Mazzotta, P., Borgani, S., Moscardini, L., Dolag, K., Tormen, G., Diaferio, A., & Murante, G. 2005, *ApJ*, 618, L1
- Read, A. M. & Ponman, T. J. 2003, *A&A*, 409, 395
- Sand, D. J., Treu, T., & Ellis, R. S. 2002, in 5 pages, 3 figures, accepted for publication in *ApJ. Letters*, 7048+
- Sand, D. J., Treu, T., Smith, G. P., & Ellis, R. S. 2004, *ApJ*, 604, 88
- Sanderson, A. J. R., Finoguenov, A., & Mohr, J. J. 2005, *ApJ*, 630, 191
- Schlegel, D. J., Finkbeiner, D. P., & Davis, M. 1998, *ApJ*, 500, 525
- Schmidt, R. W., Allen, S. W., & Fabian, A. C. 2001, *MNRAS*, 327, 1057
- Sereno, M., De Filippis, E., Longo, G., & Bautz, M. W. 2006, *ApJ*, 645, 170
- Sérsic, J. L. 1968, *Atlas de galaxies australes* (Cordoba, Argentina: Observatorio Astronomico, 1968)
- Spergel, D. N. & Steinhardt, P. J. 2000, *Physical Review Letters*, 84, 3760
- Squires, G., Kaiser, N., Babul, A., Fahlman, G., Woods, D., Neumann, D. M., & Böhringer, H. 1996, *ApJ*, 461, 572
- Stuhlinger, M., Sembay, S., Read, A. M., Baskill, D., Haberl, F., Freyberg, M. J., Dennerl, K., Kaastra, J., et al. 2006, *Status of XMM-Newton instruments' cross-calibration with SASv6.5*, Tech. Rep. XMM-SOC-CAL-TN-0052, XMM-Newton Science Operations Center
- Subramanian, K., Cen, R., & Ostriker, J. P. 2000, *ApJ*, 538, 528
- Sun, M., Forman, W., Vikhlinin, A., Hornstrup, A., Jones, C., & Murray, S. S. 2004, *ApJ*, 612, 805
- Sun, M., Jones, C., Murray, S. S., Allen, S. W., Fabian, A. C., & Edge, A. C. 2003, *ApJ*, 587, 619
- Tamura, T., Kaastra, J. S., Peterson, J. R., Paerels, F. B. S., Mittaz, J. P. D., Trudolyubov, S. P., Stewart, G., Fabian, A. C., et al. 2001, *A&A*, 365, L87
- Townsend, L. K., Broos, P. S., Garmire, G. P., & Nousek, J. A. 2000, *ApJ*, 534, L139
- Tremaine, S., Richstone, D. O., Byun, Y., Dressler, A., Faber, S. M., Grillmair, C., Kormendy, J., & Lauer, T. R. 1994, *AJ*, 107, 634
- Tyson, J. A., Kochanski, G. P., & dell'Antonio, I. P. 1998, *ApJ*, 498, L107
- Udomprasert, P. S., Mason, B. S., Readhead, A. C. S., & Pearson, T. J. 2004, *ApJ*, 615, 63
- Vikhlinin, A. 2006, *ApJ*, 640, 710
- Vikhlinin, A., Kravtsov, A., Forman, W., Jones, C., Markevitch, M., Murray, S. S., & Van Speybroeck, L. 2006, *ApJ*, 640, 691
- Vikhlinin, A., Markevitch, M., & Murray, S. S. 2001, *ApJ*, 551, 160
- Vikhlinin, A., Markevitch, M., Murray, S. S., Jones, C., Forman, W., & Van Speybroeck, L. 2005, *ApJ*, 628, 655
- Voigt, L. M. & Fabian, A. C. 2006, *MNRAS*, 368, 518
- Voit, G. M. & Donahue, M. 2005, *ApJ*, 634, 955
- Williams, L. L. R., Babul, A., & Dalcanton, J. J. 2004, *ApJ*, 604, 18
- Wise, M. 1997, *Chandra News*, 5, 22
- Zaroubi, S., Squires, G., de Gasperis, G., Evrard, A. E., Hoffman, Y., & Silk, J. 2001, *ApJ*, 561, 600
- Zaroubi, S., Squires, G., Hoffman, Y., & Silk, J. 1998, *ApJ*, 500, L87+